# Study on Terahertz Bolometer with High-Impedance Antenna

Doctor Thesis

# Study on Terahertz Bolometer with High-Impedance Antenna

Arie Pangesti Aji

Graduate School of Science and Technology
Department of Nanovision Technology

Shizuoka University
Japan

June, 2022

Doctor Thesis

# Study on Terahertz Bolometer with High-Impedance Antenna

高インピーダンス・アンテナを有するテラヘルツ用ボロメータの研究

アリ パンゲステイ アジ

静 岡 大 学

大学院自然科学系教育部

ナノビジョン工学専攻

2022 年 6 月

## *Abstract*

Frequency spectrum from 0.1 to 10 THz has been associated with the terahertz (THz) range. It is the transition region from radio−electronics to photonics. In the frequency range around 1 THz, the intermolecular vibration of prevalent molecules and chemicals formed a unique absorption characteristics known as the THz fingerprints. This distinctive feature has aroused great interest among many scientists, leading to advances in the THz research and development. Numerous THz applications are emerging in the recent decade such as the next generation high-speed wireless communication, non-destructive testing, food and water inspection, cancer detection in human tissue, and remote sensing for weather forecast. However, the lack of commercially available high-power sources and high-sensitivity detectors have made this region also known as the "THz gap" in terms of the radiating and sensing capability. Therefore, the development of high-performance THz sources and detectors is necessary.

As one of kind THz detectors, thermal detector is favorable due to the small wavelength dependency, low cost, and room-temperature operation. Sensitivity of thermal detectors is affected by the thermal conduction to the supporting structures such as substrate and the surrounding environment. Hence it is important in the design of thermal detectors to assure low

thermal conduction by making a suspended structure with long and narrow supporting legs. However, longer wavelength in the THz region makes such thermal isolation difficult, and the antenna-coupled detector becomes a viable solution, in which only the heater/thermistor part is thermally isolated.

A novel THz bolometer consisting of antenna and suspended titanium heater/thermistor on oxidized silicon substrate has been studied. Previously, the meander thermistor with fourfold higher resistance could attain twofold higher responsivity compared to the straight one. However, the heater resistance was kept low considering the impedance matching with a low-impedance half-wave dipole antenna. As a result, the noise equivalent power (NEP) could not be improved (reduced) due to the high thermal conductance of the low-resistance heater, although the responsivity was improved.

In this study, a further enhancement is attempted by introducing high-resistance heater with narrow width. To maintain optimum power transfer between antenna and heater, high-impedance folded-dipole antenna (FDA) has been introduced. Firstly, for various number of arms $N$, antenna width $W_a$, and space between arms $S$, the antenna impedance is simulated to adjust the antenna length so that the imaginary part of the impedance

becomes zero, and to obtain the resonance resistance Rr. Secondary, the absorption efficiency for the heater resistance $R_r$ is simulated to calculate the product of the efficiency and the $R_r$, which is the figure of merit (FOM) under the assumption that the thermal resistance is proportional to the heater resistance. The optimum FOM, which is 15 times larger than that of the half-wave dipole antenna, is obtained for $N$=3, $W_a$=1μm, $S$=4μm and $R_r$= 675 Ω.

The proposed design is then fabricated with electron beam lithography. Multiple devices with different heater resistances ranging from 92 to 1122 Ω are prepared. Electrical characterization reveals that the responsivity and NEP can be enhanced by a factor of 2.5 as the result of the increase in heater resistance. Furthermore, optical characterization of the FDA-coupled and half-wave dipole antenna-coupled bolometers by 1-THz source is performed by illuminating the bolometer chip installed in a vacuum dewar, with the optical input power calibrated by a commercial pyroelectric detector at the same position. In this measurement, the heater resistance is optimized separately for both kinds of antenna. As a result, the FDA coupled with the high resistance heater can realize higher responsivity and lower NEP by a factor of 1.6 compared to the half-wave dipole antenna coupled with low resistance heater. Optical measurement

with various heater resistance confirms the effective power transfer by proper impedance matching between the antenna and heater.

In addition, the bolometer thermal parameter analysis is attempted based on a simple thermal equivalent circuit model. The total thermal resistance of the bolometer consisting of the heaters with various electrical resistances and other part with a fixed thermal resistance is assumed. The extracted thermal resistance of the proposed model reproduces the electrical measurement results well. As for optical measurement, a model is proposed, in which the antenna is regarded as a voltage source with an internal resistance. The model can qualitatively explain the behavior of the optical responsivity and NEP with respect to the heater resistance for both types of antenna.

In conclusion, the comprehensive electrical and optical characterizations in this study suggests the importance of the higher heater resistance for simultaneous enhancement of responsivity and NEP in the bolometer. Application of high-impedance antenna is also important for the optimum power transfer between antenna and heater in optical characterization. The fitting results extracted by the proposed model reveals the importance of thermal conductance reduction by eliminating the thermal conduction by the parts other than the heater. This could be accomplished by the use of a

single metal film as an integrated heater and thermistor as well as removing the silicon dioxide inter- and bottom-layers.

## *Acknowledgment*

Firstly, I would like to thank the Almighty God for the blessing and grace, so this doctoral thesis can be completed on time.

My sincere gratitude to my advisor Prof. Hiroshi Inokawa for the continuous support during my 3 years of PhD study, for his patience, motivation, and immense knowledge. His guidance helped me in all the time of research and writing of this thesis, even in the very difficult situation. I could not have imagined having a better advisor and mentor for my PhD study other than him.

I would like to deeply thank Prof. Norihisa Hiromoto, Prof. Eko Tjipto Rahardjo, and Dr. Catur Apriono for introducing me to the double degree program in Shizuoka University and Universitas Indonesia, and for giving me the chance to continue my study here. I will always be indebted to you.

I also would like to send my gratitude to the members of my dissertation committee: Prof. Jun Kondoh, Prof. Tetsuo Sasaki, and Asoc. Prof. Saroj Tripathi for the encouragement in improving the quality of my PhD work.

My sincere thanks also go to Assistant Prof. Hiroaki Satoh for being my great tutor during my PhD journey, especially during device

fabrication. I will always be remembered of your kindness and patience. Thank you very much for supporting me throughout the duration of my PhD.

I would like to thank my family: my wife, my son, my parents, my brother, for supporting me spiritually throughout this PhD research and my life in general.

Finally, I would like to thank all the Inokawa-Satoh lab members for the support during the seminar and experiment in the lab. Special thanks to Mr. Shu Takeuchi, Mr. Kosuke Kusagaya, Mr. Mikihito Yoshida, Ms. Revathi Manivannan and Ms. Alka Singh.

Hamamatsu, June 2022

Arie Pangesti Aji

## *Table of Contents*

*Chapter 1*

# INTRODUCTION

## 1.1 Properties of Terahertz Radiation

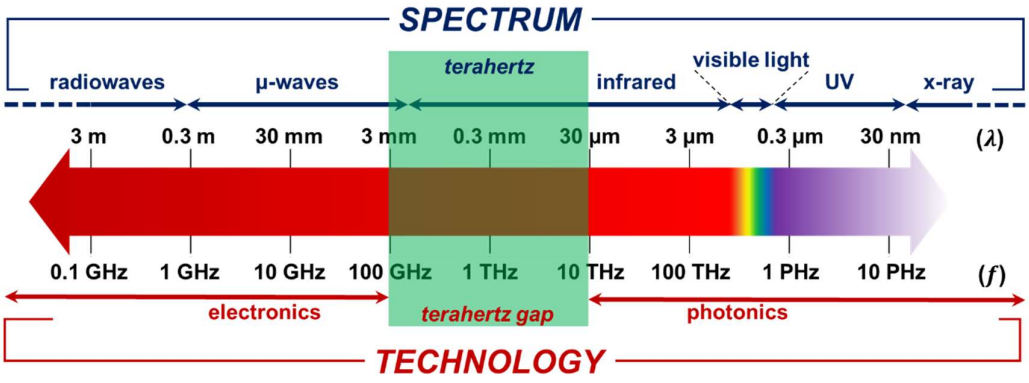


**Fig. 1-1 Spectrum of electromagnetic radiation.**

Fig. 1-1 illustrates the electromagnetic spectrum in nature. The longer wavelength region belongs to the radio- and micro-waves spectrum where electronic-based technology is used. Shorter wavelength region belongs to the infrared, visible, UV, and further X- and Gamma-rays where photonic-based devices are applied. The regions above 100 μm and below 1 mm wavelengths are technologically matured as numerous commercial sources and detectors are available on the market.

Terahertz (THz) region was originally referred to the spectrum wavelength range between 1000 to 100 μm (0.3 to 3 THz frequency) two

decades ago [1]. It has been extended into the broader spectrum overlapping with those from the sub millimeter and long-infrared wavelength regions (0.1 to 30 THz) [2]. Those newly associated THz frequency range was included due to blurred border in the transition range between radio waves and photonics domain [3]. In the research point of view, a "THz-gap" is referred to the THz region due to the lack of practically suitable technologies to commercially develop THz sources and detectors. An artificially made materials and metamaterials has been studied to fill this gap, along with newly developed photonic and electronic system for THz waves generation and detection [4][5].

Initially, THz spectroscopy was used by chemists in the spectral characterization of the rotational and vibrational resonances of simple molecules and astronomers to trace gases in the upper atmosphere. However, strong ambient moisture absorption in the wide spectral THz frequency range creates a big challenge for the THz remote sensing in the Earth's atmosphere and long-distance communication systems, as shown in Fig. 1-2. Nevertheless, strong absorbance by water at the frequency near 1 THz is advantageous for the exploration of various applications in the biomedical or food industry where the humidity measurements take place. At around 1 THz frequency region, the intra- and inter-molecular vibration

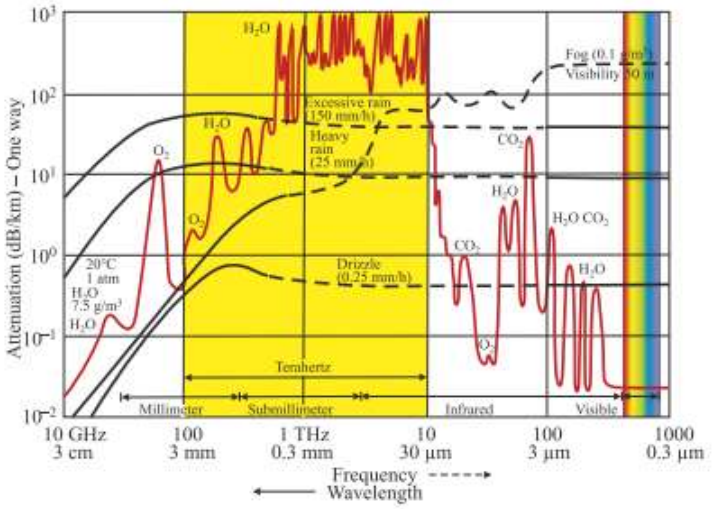


**Fig. 1-2 Attenuation of earth's atmosphere in THz region** [3].

of prevalent molecules and chemicals formed the unique absorption characteristics known as the "THz fingerprints". This distinctive feature has been studied by many scientists to advance the THz technology research and development. Numerous THz applications are emerging in the recent decade, from biomedical perspective to agricultural and food industry. Most of the applications were taking the advantage of the radiation properties of THz waves into human body and natural or artificial matters. A stronger absorption coefficient of brain gliomas is observed compared to the normal tissues at THz frequency range which is the intrinsic properties of brain tissues in THz range [6]. Another example is the screening and identification of various carbohydrates where THz time domain spectroscopy were applied in pellet form of sugar samples as shown in Fig. 1-3 [7]. Those distinct THz fingerprint spectra are beneficial

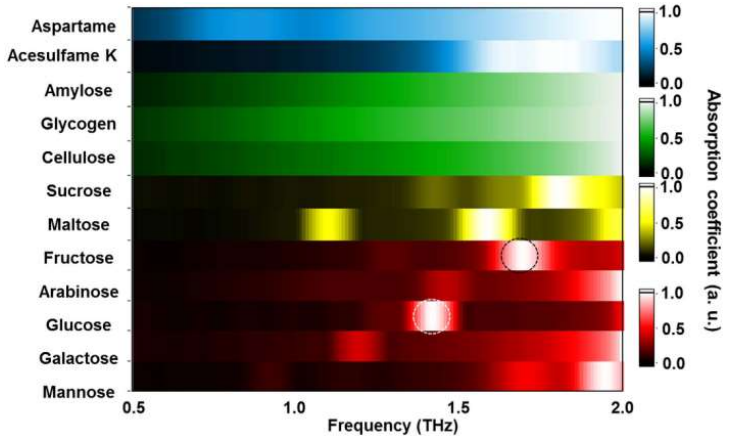


**Fig. 1-3 THz fingerprint for ten different saccharides and two non-saccharide sweeteners** [7].

for the material (solids, liquids, and gases) characterization and recognition by THz detectors are possible.

Generally, THz radiation has the photon energy of 100 meV to ~ 0.4 meV, tracked back from the blackbody radiation temperatures of ~10 K. The low energy characteristics of THz waves is advantageous for the applications where human interaction is needed. The unique radiation characteristics or properties of THz waves can be summarized as follow [8][9]:

***Penetration***

THz signals has a good penetration capability to many dielectric materials and non-polar liquids for imaging of opaque materials or objects. Clothing, paper, cardboard, wood, plastic and ceramic, are among the

materials that can be penetrated by THz waves, where they generally opaque at another spectrum wavelengths [10]–[13]. However, the low penetration depth is challenging because typically THz waves can only go through in just a few hundred microns. Some studies proposed the utilization of penetration-enhancing agents for depth improvement of THz waves penetration [14], [15].

***Non-ionization***

The photon energy at 1 THz is only 4 meV. It is much lower than the energy radiated by the X-ray waves [16]. Therefore, THz waves will not cause the light photoionization of the living tissues and DNAs. The exposure of THz waves is considered to be safe for the application that needs human as the operator or target [17], [18]. Thus, THz waves can be a better replacement for the X-rays technology for biomedical imaging or human body screening applications [19].

***Resolution***

Imaging applications require a microscopic resolution. Biomedical imaging of human cells demands submicron resolution due to cell size smaller than 10 mm. Since the resolution of an imaging system is inversely proportional to the operation wavelength, THz waves is better compared to

the microwave-based imaging. Spatial resolution as small as hundreds of nanometer scale can be achieved by the THz imaging system [20].

***Intensity***

Wave collimation in THz region is easier compared to the neighboring region such as microwave due to high spatial intensity [21]. This benefit enables the operational of THz waves apparatus in line-of-sight distance between source and target.

***Spectroscopy***

Some molecules and chemicals matter in variety poisons, illicit drugs, and explosives have the THz spectral absorption fingerprints that can be used for the identification of such materials [22]. THz-Time Domain Spectroscopy is superior to the Fourier transform infrared (FTIR) spectroscopy, as it is insensitive to the thermal background. It allows the extraction of the absorption coefficient and the refractive index [23].

## 1.2 Applications of Terahertz Radiation

Unique and distinctive properties of THz radiation have led to the development of numerous applications in wide area. In this sub-chapter, some applications in THz field will be discussed.

### *1.2.1 Security System*

The penetration capability to materials feature has made THz radiation suitable for the imaging system for security purpose, such as identification of concealed objects. Fig. 1-4 shows the scan results of a briefcase containing various items including a knife. The image was scanned with a 0.2 THz CW wave from a Gunn diode oscillator as the radiation sources and a Golay cell as the detector. The briefcase surface was surrounded by a non-conductive material that is transparent to THz radiation. The metal knife inside the briefcase blocks the THz radiation and can be well recognized as silhouettes [24]. This example is advantageous for scanning the passenger items in vital places such as airports and public area buildings, if the target material is able to block the THz waves. However, the detection might not be useful if the scanned object is covered by the harmless metallic object as the THz waves will be reflected. In addition, the non-invasive characteristics of THz waves is safe for the exposure to human tissues. Hence body scanning application with THz radiation is feasible. Fig. 1-5 shows the security screening system in reflection mode proposed by [25]. The imaging process works by irradiating the object area (i.e. human body) with multiple sub-THz radiation sources and colleting the reflected radiation by the objective lens. Imaging is then performed by the camera. With this configuration, the

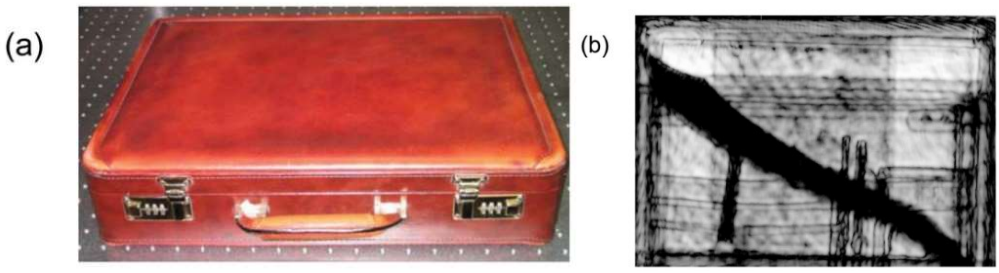


**Fig. 1-4 THz imaging for concealed object identification: (a) Briefcase made of nonconductive material that transparent to THz waves, (b) Knife inside the briefcase that blocks the THz waves and recognized as a silhouette** [24]**.**

scanner is able to reveal hidden objects at a standoff distance between 3 to 6 m from objective lens. The generator and collimating lens position and orientation have to be adjusted to make sure the incident radiation from all radiation sources converges in the area of interest, such as human body chest.

### *1.2.2 Wireless Communication System*

The lack of remaining available spectrum and bandwidth in microwave region has challenged many researches to exploit the new spectrum for the next generation wireless communication technology. Terahertz waves are like radio frequency (RF) waves in many respects. Shorter wavelength compared to microwave region highly affects the transmitter

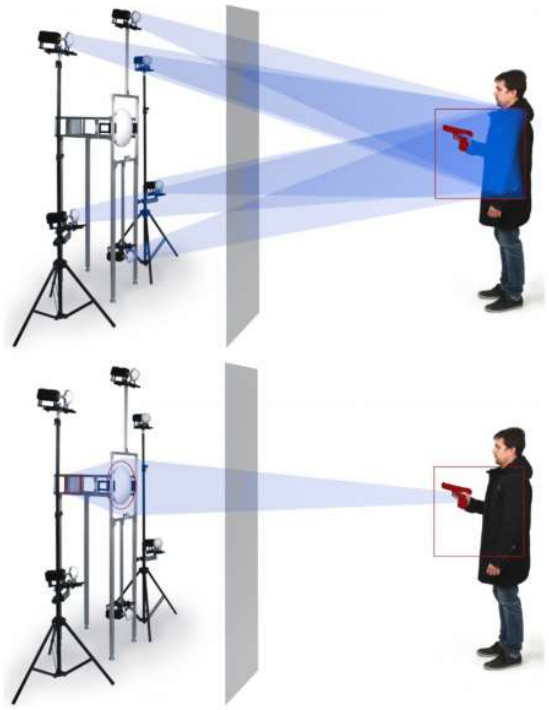

**Fig. 1-5 Scanning operation of THz imaging in reflection mode. Top: the area of interest in the human body is illuminated with sub-THz radiation from different angles. Bottom: the reflected radiation wave is collected by the objective lens and projected onto the imaging camera** [25]**.**

characteristics such as beam directivity, diffraction limit, and other antenna properties [26]. A higher frequency provides higher data rates and bandwidth to fulfil the increasing demands [27]. A 120 GHz wireless link has been proposed and tested with the maximum data rates of 10 Gbps at transmission distance of 5.8 km, opened a prospective for a high data

transmission rate in medium distance [28]. Other research has also been reported using 300 GHz frequency with the maximum data rates of 12.5 Gbps [29]. As the carrier frequency increase to several hundreds of GHz, the demand of available spectrum and wider bandwidth could be resolved.

### *1.2.3 Food and Water Control*

THz technology can also be utilized for the sensing of food and water in the food and agricultural industry, respectively. Detection of moisture content inside the food has been reported as a quality control system [30]. Detection of water content in plant leaves has been reported by a THz spectroscopy to control water supply in plants [31]. Quality control of vegetables and fruits has also been reported by utilizing the sensitivity of THz technology to temperature, soluble solid content, moisture content inside the fruit [32], [33]. Furthermore, the same application can also be used for the extraction of the refractive index and absorption coefficient of the sucrose solution in fruits.

### *1.2.4 Biomedical Applications*

The non-ionizing property of THz waves confirms its potential for medical applications. Less risk to patient health is expected due to lower photon energy compared to the old medical devices based on the UV and X-ray waves. Hence various diseases can be diagnosed by irradiating the

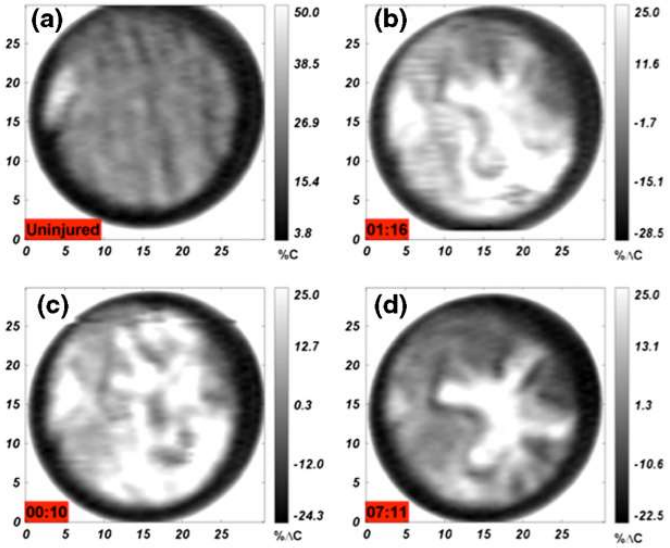


**Fig. 1-6 THz imager for the detection of rat skin burn degree. (a) Uninjured skin without any burn; (b) 10 min after burn; (c) burned more than 1 hours; (d) more than 7 hours burned skin with highest reflective signals** [34]**.**

human target body with THz waves. Fig. 1-6 shows the example of a THz imager to identify the degree of a burned rat skin by *in vivo* experiment. The analysis was taken by the reflected radiation from a normal skin until it burned for about 8 hours, resulting in a light area with high reflected signals. Further examination can also be expected for human skin burn detection [34]. 3D imaging by TDS system has been reported for early detection of skin cancer by penetrating the THz radiation into human skin up to 1.2 mm deep [35]. Certain biomolecules identification and

classification are still widely opened by utilizing THz spectroscopy with high efficiency and accuracy. The THz technology for biomedical applications have brought huge benefits for the medical research and industry [36].

## 1.3 Type of THz Detector

General classification of THz detectors is cooled and uncooled. Cooled detectors demand for cooling mechanism below ambient temperatures. They offer significant benefit in terms of range, resolution, and high sensitivity. Increasing demand for low cost, smaller size, light weight, longer lifetime, and low power THz detectors have made the uncooled THz detectors are more favorable to be studied and developed. Another distinct classification method is based on the detection mechanism which will be discussed in the following sub chapters.

### *1.3.1 Photon Detector*

In photon detectors, absorption of the incident radiation within the material is done by the interaction with electrons that either bound to lattice atoms, impurity atoms or with free electrons. The electrical output signal was resulted from the energy distribution change [37]. The photon detectors have the wavelength selectivity characteristics response per unit incident radiation power because the energy of incident photon should

exceed the energy level difference to generate a carrier. As the energy per photon is inversely proportional to the wavelength, the spectral response of photon detectors increases linearly with increasing wavelength up to the cutoff wavelength which determined by the detector material. Photon detector is suitable for the detection in the far-IR region. However, at THz region it is strongly limited by the thermal energy of the carrier hence it is not applicable to be used at room-temperature. The photon energy of 4 meV at 1 THz is very low compared to the thermal energy of 26 meV, assuming room temperature operation [3]. Common material used in photon detector is cadmium mercury telluride (HgCdTe) due to their bandgap tailoring characteristics. However, it requires high cost for the growth and processing [38]. As the main disadvantage of photon detectors came from the cooling requirement to prevent thermal generation in charged carriers, thermal detectors are more applicable for the application in long wave infrared and THz region.

### *1.3.2 Thermal Detector*

The basic principle operation in thermal detectors is the absorbed incident radiation causes a temperature change in the detector material. The temperature change also leads to the material property changes, hence the output can be measured electronically. Typically, thermal detectors can be

operated at a room temperature. They are characterized by its moderate sensitivity and slower response compared to the photon detectors because heating and cooling process of a detector element is relatively a slow process. However, they are low cost and easier to be used. Bolometers, pyroelectrics, and thermopiles are among the most studied thermal detectors.

Bolometer is a kind of thermal detector where the electromagnetic radiation is detected as a change in resistance of the sensing element. In bolometer, the energy of the absorbed THz radiation is transferred to the sensing element's crystal lattice, resulting in temperature increase. Therefore, the response depends on the temperature coefficient of resistance (TCR) of the detector materials [39]. The selection for detector's sensing material is important to improve the detector sensitivity. As the detected signal will be changed per degree of temperature, it is important to have a material with a high TCR. Vanadium oxides ($VO_x$), amorphous silicon (α-Si) and $p^+$/n-well silicon are the most common materials used in the uncooled detectors [40]–[42]. Resistive microbolometers were widely used to detect radiation in the long wavelength region of IR and THz spectrum. They are usually implemented by suspended bridge configuration for improve the thermal insulation [43].

Recently, metal bolometers have been intensively studied as an alternative material. Metallic bolometers made of bismuth (Bi) or titanium (Ti) have relatively small bulk TCR than high-TCR materials like VOx and α-Si. However, they have lower shot and thermal noises [44]. The performance of a metal bolometer is beneficial in the case of relatively higher TCR achieved by any design methodology. Ti has several advantages, such as: (i) low thermal and electrical conductivity, (ii) invulnerability to electromigration, (iii) low flicker noise, (iv) compatible with Silicon wafer processing technology, and (v) it does not deteriorate with time of operation [45], [46]. Some notable Ti-based microbolometer has been studied with promising high responsivity and low noise performance [47], [48].

### *1.3.2 Electronic Receivers*

The third class of THz detector is based on the electronic receivers. In the photon and thermal based detectors, they are considered as the traditional THz detector that limited by the cooling requirements, system complexities, response time, and cost. Those obstacles have restrained the possibility of the photon- and thermal-based detectors to a majority of commercially deployable THz applications. Researchers has begun to seek for the prospect in developing THz detector which based on the integrated

circuit design in solid state industry. Depending on their functions and circuit types, electronic receiver detectors can also be divided into direct and heterodyne detection. In a direct detection, THz radiation is directly absorbed by the sensitive elements leading to rectification processes. As for heterodyne detection, the THz radiation signal is down converted to the intermediate frequency (IF) band by a nonlinear element such as mixer and local oscillator. Furthermore, the output IF signal is processed using additional electronic devices. CMOS and SiGe HBT technologies have emerged in the last decade as they are advance in Si processing technology, design technique, and micro electro mechanical system (MEMS) packaging. Numerous research in the complex THz integrated circuits have expanded the THz applications into prospective new fields in terms of passive and active imaging system. The passive imaging system detects and measure the naturally available energy. While the active imaging provides their own radiation energy source for illumination to be directed towards the observed target and the reflected radiation is then detected and measured by the sensor [49]. A passive monitoring has been reported by NASA Jet propulsion Laboratory, which utilize 675 GHz heterodyne RF electronic blocks for the low-distortion, fast beam scanning, and a real-time radar image in personnel identification application [50]. A GaN-based asymmetric nanodiodes have been studied as direct and heterodyne

detectors up to 0.69 THz which promising for the low-cost solution and the mounting simplification [51]. As for the rectification-based THz direct detectors include the application of MOSFET [52], pn-Diode [53], Schottky barrier diode (SBD) [54], and high electron mobility transistor (HEMT) [55]. The advantage of the direct detectors over the heterodyne is their practical simplicity. However, heterodyne detectors show better sensitivity [56].

Direct detectors in the electronic receiver are faster and it also suitable for room temperature operation. However, some challenges exist in their intrinsic cutoff frequency as well as the increasing parasitic effects in the THz frequency, and the performance tends to degrade rapidly with frequency [57]. Therefore, thermal detector such as bolometer which also based on the direct detection mechanism with relatively insensitive performance to the frequency still have some usefulness in the detection of THz waves. Table 1.1 shows the comparison between THz direct detectors of electronic receiver- and thermal-based detectors.

## 1.4 Scaling Study of Terahertz Bolometer

An antenna-coupled bolometer is the THz thermal detector utilizes antenna as the radiation receiver element rather than direct absorption by the bolometer sensor [58]. It is commonly used by the detector operating

**Table 1.1 THz direct detector comparison between electronic receiver and thermal-based detectors**

| Detector type | Sensor | Antenna | Freq (THz) | Rv (V/W) | NEP (pW/$\sqrt{Hz}$) | Resp. time | Ref. |
|---|---|---|---|---|---|---|---|
| Electronic | MOSFET | Loop | 1 | 765 | 25 | 0.3 s | [52] |
| Electronic | pn-Diode | Patch | 0.78 | 558 | 56 | - | [53] |
| Electronic | SBD | Bowtie | 0.22 | 2200 | 2.6 | - | [54] |
| Electronic | HEMT | Dipole | 0.85 | 4 A/W | 0.3 at 77 K | 0.2 s | [55] |
| Thermal | Ti bolometer | Dipole | 1 | 90 | 460 | - | [59] |
| Thermal | VOx bolometer | Patch | 2.5 | 1235 | 87.4 | - | [60] |
| Thermal | YBCO bolometer | Log-spiral | 0.4 | 45 | 50 | - | [61] |
| Thermal | Nb5N6 bolometer | Slot | 0.64 | 113 | 44 | - | [62] |

in the wavelength region that relatively longer than the optimal size of the sensing element to reduce the thermal capacitance and conductance. A novel THz bolometer has been proposed by separating heater and thermistor structure on top of Si substrate [63]. The incident THz radiation is received by antenna, and the induced current heats up the load resistor (heater). Temperature rise caused by the heater is then detected by a thermistor (temperature-sensitive resistor). This model is suitable for the detection of THz waves, as only the part of the integrated heater and thermistor are thermally isolated, and the larger THz antenna part can be adjusted and fabricated without any difficulties. Furthermore, the heater

and thermistor could be independently scaled and optimized for highest possible responsivity.

In the initial design of the antenna-coupled microbolometer, a straight thermistor and heater was applied. It is revealed that longer thermistors have higher responsivity due to better thermal isolation and low thermal loss [64]. As the thermistor length is limited by the size of the antenna gap, further improvement was made by scaling down the thermistor. The first scaling study revealed the responsivity improvement by increasing thermistor resistance with a fixed heater resistance. The meander thermistor was then applied with a longer effective length as the miniaturization technique to keep the lateral length the same as heater in the antenna gap. A scaled down thermistor with effective length of 20 μm and 10 μA bias current was studied and the responsivity could be improved up to four times compared to the straight device [65]. Longer thermistor of 90 μm with a narrow width of 0.1 μm has been proposed with a more complex meander structure resulting in responsivity improvement up to 787 V/W under 50 μA bias current [66]. Note that in the two initial scaling studies, the heater dimensions were kept the same to maintain the low impedance characteristics of the halfwave dipole antenna. However, it was also found that the noise equivalent power (NEP) performance was

**Table 1.2 Scaling study of the detector where thermistor resistance is scaled up but heater is fixed** [66]**.**

| Parameters | Scaling Factor | Remarks |
|---|---|---|
| Thermistor resistance ($R_{th}$) | λ | Resistance increase by meander shaped thermistor |
| Heater resistance ($R_h$) | 1 | Fixed heater dimension |
| Thermal conductance ($G_{th}$) | 1 | Kept constant by the heater conductance |
| Bias current ($I_b$) | $1/\lambda^{1/2}$ | To maintain a fixed ΔT |
| Temperature rise (ΔT) | 1 | Kept constant to assure reliability |
| Thermistor TCR (α) | 1 | Material properties assumed independent |
| Responsivity ($R_v$) | $\lambda^{1/2}$ | $R_{th} \times I_b \times \alpha / G_{th}$ |
| Noise voltage ($V_n$) | $\lambda^{1/2}$ | $(4 \times k_B \times T \times R_{th})^{1/2}$ |
| Noise equivalent power (NEP) | 1 | $V_n/R_v$ |

detrimental and could not be simultaneously reduced if the heater resistance is fixed, as shown in Table 1.2. Note that the noise of the detector is originated mostly from the thermal noise generated in thermistor. Therefore, scaling the thermistor resistance up by changing its dimensions led to the fixed NEP because thermal conductance of detector, which dominated by the heater, was kept the same.

**Table 1.3 Scaling study of the detector where thermistor and heater resistance are uniformly scaled up** [66]**.**

| Parameters | Scaling factor | Remarks |
|---|---|---|
| Thermistor resistance ($R_{th}$) | λ | Resistance increase by meander shaped thermistor |
| Heater resistance ($R_h$) | λ | Resistance increase by narrow width or thinner heater |
| Thermal conductance ($G_{th}$) | 1/λ | Inversely proportional to $R_h$ based |
| Bias current ($I_b$) | 1/λ | To maintain a fixed ΔT |
| Temperature rise (ΔT) | 1 | Kept constant to assure reliability |
| TCR (α) | 1 | Material properties assumed independent |
| Responsivity ($R_v$) | λ | $R_{th} \times I_b \times \alpha$ / $G_{th}$ |
| Noise voltage ($V_n$) | $\lambda^{1/2}$ | $(4 \times k_B \times T \times R_{th})^{1/2}$ |
| Noise equivalent power (NEP) | 1/λ | $V_n/R_v$ |

Further improvement in the NEP is proposed by the second scaling study where the heater is proportionally scaled down with thermistors (resistance increase), as shown in Table 1.3. As shown, a uniform resistance increase in thermistor and heater is important to reduce the thermal conductance of the bolometer. With this manner, the thermal conductance of bolometer is scaled down as it is inversely proportional to

the heater resistance. Resistance increase in thermistor was attained by using meander structure, with longer effective length that could improve the responsivity but detrimental to the NEP performance. While for the heater, as the gap between the antenna is fix, resistance increase could be realized by the reduction of width or thickness. Increasing heater resistance will lead to the responsivity improvement as well as reduction of NEP, as the voltage noise in detector is solely dominated by thermal noise in the thermistor device. However, as the heater is coupled to the antenna, heater resistance increase requires a change in the antenna resistance as well. Halfwave dipole antenna that commonly used has relatively low impedance characteristics around 40 Ω, so it can only be optimally coupled with a low resistance heater. Therefore, further improvement in the heater resistance should be followed by the development of the antenna with higher impedance with the same resonant frequency.

## 1.5 High-impedance Antenna Overview

In a wireless communication system with a typical high input or output impedance characteristics requires the application of an equivalent impedance antenna to efficiently transmit and/or receive the electromagnetic radiation. When an antenna with moderate input impedance is applied to a high impedance device, the power transfer to the

antenna is limited due to the impedance mismatch. Impedance matching between the high resistance transmitter device and the antenna can be enhanced by improving the antenna resistance, to increase power radiated from the antenna. Classic resonant type of antennas, such as half-wavelength dipole, full-wavelength dipole, and slot antennas, with the moderate resistance have been used primarily for low power CW applications. Photomixer is one of the devices with a high-impedance characteristics required for a photoconductive antenna where the typical output impedance is extremely high [67]. A room-temperature thermal detectors and focal-plane arrays (FPAs) imaging system with typical high-impedances at frequencies around 1 THz have been reported using semiconductor devices, such as Schottky diodes and heterostructure backward diodes (HBDs) [68]–[70]. The considerable impedance mismatch between devices and classic planar antennas resulting in the limited power coupling efficiency thus impact in relatively low detector performance. Impedance matching networks can be applied, but this will inevitably lead to the larger size, complex systems, and reduced bandwidth detection [71]. To overcome these issues, high embedding impedance antennas are needed.

Increasing the effective length of a dipole antenna will improve its impedance. Among various planar type antenna, meander structure antenna is promising and applicable to be used with the high-impedance devices. Low profile, easy to fabricate, and tunability of a meander shaped planar antenna are advantageous for the application in THz detectors. Folded dipole antenna (FDA) has long been used for the high resistance application in the photomixers as well as infrared detectors. FDA can be constructed by folding a λ/2 long element, that is basically a two-wire transmission line [72]. Since the folded dipole length can be considered as a λ-long loop antenna, the antenna can be referred as a folded loop, either open or closed. Furthermore, the impedance of FDA can be adjusted by changing the width or the spacing between the antenna arms. Typical impedance of an FDA can be designed up to four times of the classic halfwave dipole antenna, with the same gap length at the center part [73]. As the resistance of absorber element in a THz detector can be varied, an FDA is applicable for the high-resistance heater in a THz microbolometer.

## 1.6 Motivation of Present Work

Terahertz technology in the frequency range between 0.1 to 10 THz have gained much attention due to the increased demand in security, biomedical, material identification and wireless communication system

applications [74], [75]. The electromagnetic wave around 1 THz is prospective for the non-invasive and non-destructive imaging due to the unique radiation properties related to the interaction of THz signals to different organic or inorganic matters. The wide scope of THz technology advances the augmentation of high sensitivity, low-cost, and room-temperature operable THz detectors. Recent thermal detector technologies, in conjunction with the latest semiconductor processing technology have ignited more exciting possibilities for the development of thermal radiation detector. Rapid progress in micromachining technology have also brought to the reduction of fabrication costs and device size, while keeping the high sensitivity performance.

The presence of numerous water absorption can also be considered as one of the key features in the THz region spectrum for biomedical application. In conjunction with the non-ionizing and non-destructive characteristics, the features of THz waves are well suited as the replacement of the legacy medical application based on X-rays. The big challenge for the researchers nowadays is to realize the technology into the market available products and appliances.

In the recent decade, there are a lot of THz sources and detectors have been studied, developed, and sold on the market. Hot electron

bolometers and superconducting bolometers have been widely used as the thermal detectors with a high radiation sensitivity. However, they require additional cooling system which make it bulky for most of the outdoor application. A solution in a room-temperature detector results in the development of Golay cell and pyroelectric based thermal detectors, with the tradeoff in inferior sensitivity. Matured technologies in radio microwave and optical infrared regions allow the development of diverse range application with room-temperature and high-sensitivity capable detectors. However, this is not the case for the THz region. Therefore, the demand is increasing for the microwave- or optical-comparable performance THz detector. General mechanism applied in a thermal detector is that the detected signal caused a change in the detector's material property as the effect of temperature rise. To preserve the thermal conduction as low as possible, the detector size must be small. THz region has a longer wavelength relative to the typical physical size of the sensing element. However, to handle the diffraction limit in THz region, the size of detector should be as large as $\lambda/n_e$ for the wavelength ($\lambda$) and effective refractive index of the supporting substrate ($n_e$) [67]. Such large detector size makes it difficult to reduce the thermal conductance and heat capacity. Antenna-coupled bolometer was then proposed to resolve this problem, to capture THz radiation with smaller detector size.

For THz passive thermal imaging applications, the noise equivalent temperature difference (NETD) is often considered as the main performance parameter. NETD is a measure of sensing the temperature difference between the background and the object. NETD of less than 1 K is required for passive imaging system [76]. However, for a single pixel detector, the noise equivalent power (NEP) is more appropriate to be considered. NETD and NEP are correlated each other by the following equation [39]

$$NEP = NETD \frac{\tau_0 A_D (\Delta P/\Delta T)_{\lambda_1-\lambda_2}}{4F^2}, \tag{1.1}$$

where $\tau_0$ is the optics transmittance between source and detector, $A_D$ is the detector area size, $(\Delta P/\Delta T)_{\lambda_1-\lambda_2}$ is the change in power per unit area radiated by a blackbody at absolute temperature of *T*, with respect to *T*, measured within the wavelength range from $\lambda_1$ to $\lambda_2$, and *F* number of the optics. Power *P(λ,T)* emitted by a blackbody can be calculated based on the Planck radiation law with the following equation

$$P(\lambda, T) = \frac{2\pi hc^2}{\lambda^5 (e^{\frac{hc}{k_B T \lambda}} - 1)} \tag{1.2}$$

where *h*, *c* and $k_B$ are Planck constant, velocity of light and Boltzmann constant, respectively. The $(\Delta P/\Delta T)_{\lambda_1-\lambda_2}$ can then be calculated as

$$(\Delta P/\Delta T)_{\lambda_1-\lambda_2} = \int_{\lambda_1}^{\lambda_2} \frac{\partial P(\lambda,T)}{\partial T} d\lambda \quad (1.3)$$

For the room temperature of 300K and target frequency of 1 THz with 10% bandwidth, $(\Delta P/\Delta T)_{\lambda_1-\lambda_2}$ is $9.69\times10^{-5}$ W/(m$^2$K). Therefore, NEP less than 2.2 pW is required for a NETD less than 1 K, if $A_D=\lambda^2$, $\tau_0=1$ and F=1 are assumed. For the present work, our objective is to develop the room-temperature 1 THz detector with high responsivity and low NEP in the order of one pW/$\sqrt{Hz}$ for passive imaging application.

Taking the advantage of our group's expertise, in this research we present the development of antenna-coupled bolometer. The research done on this thesis can be briefly summarized as follows:

1. Design and simulation of a folded dipole antenna to attain high-impedance characteristics. As the heater part in the THz detector should be scaled down to increase its resistance, development of a 1 THz resonant capable folded dipole antenna is proposed. We designed and simulated the folded dipole antenna by changing its basic dimension parameters such as length, width, spacing, and the number of arms. A commercial electromagnetic simulator was used for this purpose. Performance parameters was evaluated based on the

impedance matching condition between the antenna and heater which gives highest absorption efficiency of the antenna.

2. Fabrication of Ti-based THz microbolometer with multiple heater width. Scaling study in Table 1-1 had been realized by a meander thermistor and a fixed heater. To further improve the responsivity and reduce the NEP, we seek to adopt the scaling study presented in Table 1-2. In order to increase the heater resistance with a fix length, variation of heater width and thickness are chosen. Evaluation of the fabricated THz detectors is performed by electrical and optical characterization. Halfwave and folded dipole antennas were studied to compare the performance between low- and high-resistance heater.

The purpose of this study is to verify the usefulness of high-impedance antenna in antenna-couple bolometer and to realized improved performance by scaling the heater resistance. The originality of this work is the systematic study of bolometer performance with respect to heater resistance for high-impedance FDA, together with low-noise metallic thermistor.

## 1.7 Synopsis of Book Chapters

In this thesis, antenna-coupled microbolometers with Ti thermistor and heater have been discussed to be realized as the THz thermal detector.

Chapter-1 presents the properties of THz waves, wide range of potential applications, overview of the THz detectors classification, scaling study of an integrated heater-thermistor structure in THz detector and possibility of a high-impedance antenna for the high-resistance heater coupled device. Finally, it presents the motivation of the present work and synopsis of book chapters.

Chapter-2, discusses the characterization of a folded dipole antenna by using electromagnetic simulator. The folded dipole antenna designed with various dimension parameters, such as length, width, spacing, and number of arms. Transmitting and receiving mode simulations have been used for the performance characterization. A fair comparison to the classic halfwave dipole is made to find the overall theoretical improvement of the folded dipole antenna for the radiation receiver in the THz microbolometer.

Chapter-3, discusses the fabrication and measurement of THz microbolometer with high-impedance antenna. Fabrication is mainly performed by the electron beam lithography (EBL) as the patterning apparatus. Electrical characterization performed by using direct AC power applied to the heater. Optical characterization performed by using THz radiation source.

Chapter-4, discusses the summary and conclusion of the present result and provides suggestion on the direction for further development in this field.

## References


[1] P. H. Siegel, "Terahertz technology," *IEEE Transactions on Microwave Theory and Techniques*, vol. 50, no. 3, pp. 910–928, Mar. 2002, doi: 10.1109/22.989974.

[2] S. S. Dhillon *et al.*, "The 2017 terahertz science and technology roadmap," *Journal of Physics D: Applied Physics*, vol. 50, no. 4, p. 043001, Feb. 2017, doi: 10.1088/1361-6463/50/4/043001.

[3] A. Rogalski and F. Sizov, "Terahertz detectors and focal plane arrays," *Opto-Electronics Review*, vol. 19, no. 3, Jan. 2011, doi: 10.2478/s11772-011-0033-3.

[4] R. Mendis *et al.*, "Terahertz Artificial Dielectric Lens," *Scientific Reports*, vol. 6, no. 1, p. 23023, Sep. 2016, doi: 10.1038/srep23023.

[5] R. Mendis, *et al.*, "Artificial dielectric polarizing-beamsplitter and isolator for the terahertz region," *Scientific Reports*, vol. 7, no. 1, p. 5909, Dec. 2017, doi: 10.1038/s41598-017-06297-7.

[6] K. Meng *et al.*, "Terahertz pulsed spectroscopy of paraffin-embedded brain glioma," *Journal of Biomedical Optics*, vol. 19, no. 7, p. 077001, Jul. 2014, doi: 10.1117/1.JBO.19.7.077001.

[7] D.-K. Lee *et al.*, "Highly sensitive and selective sugar detection by terahertz nano-antennas," *Scientific Reports*, vol. 5, no. 1, p. 15459, Dec. 2015, doi: 10.1038/srep15459.

[8] D. L. Woolard, R. Brown, M. Pepper, and M. Kemp, "Terahertz Frequency Sensing and Imaging: A Time of Reckoning Future Applications?," *Proceedings of the IEEE*, vol. 93, no. 10, pp. 1722–1743, Oct. 2005, doi: 10.1109/JPROC.2005.853539.

[9] K. R. Jha and G. Singh, "Terahertz planar antennas for future wireless communication: A technical review," *Infrared Physics & Technology*, vol. 60, pp. 71–80, Sep. 2013, doi: 10.1016/j.infrared.2013.03.009.

[10] A. Y. Pawar, D. D. Sonawane, K. B. Erande, and D. v. Derle, "Terahertz technology and its applications," *Drug Invention Today*, vol. 5, no. 2, pp. 157–163, Jun. 2013, doi: 10.1016/j.dit.2013.03.009.

[11] G.-H. Oh, H.-S. Kim, D.-W. Park, and H.-S. Kim, "In-situ monitoring of moisture diffusion process for wood with terahertz time-domain spectroscopy," *Optics and Lasers in Engineering*, vol. 128, p. 106036, May 2020, doi: 10.1016/j.optlaseng.2020.106036.

[12] D. Zimdars and J. S. White, "Terahertz reflection imaging for package and personnel inspection," in *Proc. SPIE 5411, Terahertz for Military and Security Applications II*, Sep. 2004, p. 78. doi: 10.1117/12.562216.

[13] D. Wu, C. Haude, R. Burger, and O. Peters, "Application of terahertz time domain spectroscopy for NDT of oxide-oxide ceramic matrix composites," *Infrared Physics & Technology*, vol. 102, p. 102995, Nov. 2019, doi: 10.1016/j.infrared.2019.102995.

[14] A. Ren *et al.*, "State-of-the-art in terahertz sensing for food and water security – A comprehensive review," *Trends in Food Science and Technology*, vol. 85, pp. 241–251, Mar. 01, 2019. doi: 10.1016/j.tifs.2019.01.019.

[15] H. Cheon, H.-J. Yang, and J.-H. Son, "Toward Clinical Cancer Imaging Using Terahertz Spectroscopy," *IEEE Journal of Selected Topics in Quantum Electronics*, vol. 23, no. 4, pp. 1–9, Jul. 2017, doi: 10.1109/JSTQE.2017.2704905.

[16] K. Wang, D. W. Sun, and H. Pu, "Emerging non-destructive terahertz spectroscopic imaging technique: Principle and applications in the agri-food industry," *Trends in Food Science and Technology*, vol. 67. Elsevier Ltd, pp. 93–105, Sep. 01, 2017. doi: 10.1016/j.tifs.2017.06.001.

[17] Q. Wang, S. Hameed, L. Xie, and Y. Ying, "Non-destructive quality control detection of endogenous contaminations in walnuts using terahertz spectroscopic imaging," *Journal of Food Measurement and Characterization*, vol. 14, no. 5, pp. 2453–2460, Oct. 2020, doi: 10.1007/s11694-020-00493-2.

[18] G. Ok, H. J. Kim, H. S. Chun, and S.-W. Choi, "Foreign-body detection in dry food using continuous sub-terahertz wave imaging," *Food Control*, vol. 42, pp. 284–289, Aug. 2014, doi: 10.1016/j.foodcont.2014.02.021.

[19] C. M. Armstrong, “The truth about terahertz,” *IEEE Spectrum*, vol. 49, no. 9, Sep. 2012, doi: 10.1109/MSPEC.2012.6281131.

[20] H.-T. Chen, R. Kersting, and G. C. Cho, “Terahertz imaging with nanometer resolution,” *Applied Physics Letters*, vol. 83, no. 15, pp. 3009–3011, Oct. 2003, doi: 10.1063/1.1616668.

[21] E. Budiarto, J. Margolies, S. Jeong, J. Son, and J. Bokor, “High-intensity terahertz pulses at 1-kHz repetition rate,” *IEEE Journal of Quantum Electronics*, vol. 32, no. 10, pp. 1839–1846, 1996, doi: 10.1109/3.538792.

[22] M. C. Kemp, “Explosives Detection by Terahertz Spectroscopy—A Bridge Too Far?,” *IEEE Transactions on Terahertz Science and Technology*, vol. 1, no. 1, pp. 282–292, Sep. 2011, doi: 10.1109/TTHZ.2011.2159647.

[23] A. G. Davies, A. D. Burnett, W. Fan, E. H. Linfield, and J. E. Cunningham, “Terahertz spectroscopy of explosives and drugs,” *Materials Today*, vol. 11, no. 3, pp. 18–26, Mar. 2008, doi: 10.1016/S1369-7021(08)70016-6.

[24] H.-B. Liu, H. Zhong, N. Karpowicz, Y. Chen, and X.-C. Zhang, “Terahertz Spectroscopy and Imaging for Defense and Security Applications,” *Proceedings of the IEEE*, vol. 95, no. 8, pp. 1514–1527, Aug. 2007, doi: 10.1109/JPROC.2007.898903.

[25] G. Tzydynzhapov, P. Gusikhin, V. Muravev, A. Dremin, Y. Nefyodov, and I. Kukushkin, “New Real-Time Sub-Terahertz Security Body Scanner,” *Journal of Infrared, Millimeter, and Terahertz Waves*, vol. 41, no. 6, pp. 632–641, Jun. 2020, doi: 10.1007/s10762-020-00683-5.

[26] J. F. O’Hara, S. Ekin, W. Choi, and I. Song, “A Perspective on Terahertz Next-Generation Wireless Communications,” *Technologies*, vol. 7, no. 2, p. 43, Jun. 2019, doi: 10.3390/technologies7020043.

[27] K. M. S. Huq, S. A. Busari, J. Rodriguez, V. Frascolla, W. Bazzi, and D. C. Sicker, “Terahertz-Enabled Wireless System for Beyond-5G Ultra-Fast Networks: A Brief Survey,” *IEEE Network*, vol. 33, no. 4, pp. 89–95, Jul. 2019, doi: 10.1109/MNET.2019.1800430.

[28] A. Hirata *et al.*, "120-GHz-Band Wireless Link Technologies for Outdoor 10-Gbit/s Data Transmission," *IEEE Transactions on Microwave Theory and Techniques*, vol. 60, no. 3, pp. 881–895, Mar. 2012, doi: 10.1109/TMTT.2011.2178256.

[29] H.-J. Song *et al.*, "Terahertz wireless communication link at 300 GHz," in *2010 IEEE International Topical Meeting on Microwave Photonics*, Oct. 2010, pp. 42–45. doi: 10.1109/MWP.2010.5664230.

[30] J. F. Federici, "Review of Moisture and Liquid Detection and Mapping using Terahertz Imaging," *Journal of Infrared, Millimeter, and Terahertz Waves*, vol. 33, no. 2, pp. 97–126, Feb. 2012, doi: 10.1007/s10762-011-9865-7.

[31] F. Qu, P. Nie, L. Lin, C. Cai, and Y. He, "Review of theoretical methods and research aspects for detecting leaf water content using terahertz spectroscopy and imaging," *International Journal of Agricultural and Biological Engineering*, vol. 11, no. 5, pp. 27–34, 2018, doi: 10.25165/j.ijabe.20181105.3952.

[32] G. Hao, J. Liu, and Z. Hong, "Determination of soluble solids content in apple products by terahertz time-domain spectroscopy," in *Proc. SPIE 8195, International Symposium on Photoelectronic Detection and Imaging 2011: Terahertz Wave Technologies and Applications*, Jun. 2011, p. 819510. doi: 10.1117/12.900671.

[33] D. Khaled, N. Novas, J. Gazquez, R. Garcia, and F. Manzano-Agugliaro, "Fruit and Vegetable Quality Assessment via Dielectric Sensing," *Sensors*, vol. 15, no. 7, pp. 15363–15397, Jun. 2015, doi: 10.3390/s150715363.

[34] P. Tewari *et al.*, "In vivo terahertz imaging of rat skin burns," *Journal of Biomedical Optics*, vol. 17, no. 4, p. 040503, 2012, doi: 10.1117/1.JBO.17.4.040503.

[35] A. Rahman, A. K. Rahman, and B. Rao, "Early detection of skin cancer via terahertz spectral profiling and 3D imaging," *Biosensors and Bioelectronics*, vol. 82, pp. 64–70, Aug. 2016, doi: 10.1016/j.bios.2016.03.051.

[36] A. Gong, Y. Qiu, X. Chen, Z. Zhao, L. Xia, and Y. Shao, "Biomedical applications of terahertz technology," *Applied Spectroscopy*

*Reviews*, vol. 55, no. 5, pp. 418–438, May 27, 2020. doi: 10.1080/05704928.2019.1670202.

[37] M. A. Kinch, "Fundamental physics of infrared detector materials," *Journal of Electronic Materials*, vol. 29, no. 6, pp. 809–817, Jun. 2000, doi: 10.1007/s11664-000-0229-7.

[38] A. Rogalski, "HgCdTe infrared detector material: history, status and outlook," *Reports on Progress in Physics*, vol. 68, no. 10, pp. 2267–2336, Oct. 2005, doi: 10.1088/0034-4885/68/10/R01.

[39] P. W. Kruse, *Uncooled Thermal Imaging Arrays, Systems, and Applications*. Bellingham, USA: SPIE Press, 2001.

[40] M. Ueno *et al.*, "Monolithic uncooled infrared image sensor with 160 by 120 pixels," in *Proc. SPIE 2552, Infrared Technology XXI*, Sep. 1995, pp. 636–643. doi: 10.1117/12.218260.

[41] A. J. Syllaios, T. R. Schimert, R. W. Gooch, W. L. McCardel, B. A. Ritchey, and J. H. Tregilgas, "Amorphous Silicon Microbolometer Technology," *MRS Proceedings*, vol. 609, p. A14.4, Mar. 2000, doi: 10.1557/PROC-609-A14.4.

[42] H. Jerominek, "Vanadium oxide films for optical switching and detection," *Optical Engineering*, vol. 32, no. 9, p. 2092, 1993, doi: 10.1117/12.143951.

[43] R. A. Wood, C. J. Han, and P. W. Kruse, "Integrated uncooled infrared detector imaging arrays," in *Technical Digest IEEE Solid-State Sensor and Actuator Workshop*, 1992, pp. 132–135. doi: 10.1109/SOLSEN.1992.228308.

[44] A. Tanaka *et al.*, "Infrared focal plane array incorporating silicon IC process compatible bolometer," *IEEE Transactions on Electron Devices*, vol. 43, no. 11, pp. 1844–1850, 1996, doi: 10.1109/16.543017.

[45] Y. L. Cheng, B. J. Wei, F. H. Shih, and Y. L. Wang, "Stability and Reliability of Ti/TiN as a Thin Film Resistor," *ECS Journal of Solid State Science and Technology*, vol. 2, no. 1, pp. Q12–Q15, Nov. 2013, doi: 10.1149/2.022301jss.

[46] J. Trontelj, G. Valušis, R. Venckevičius, I. Kašalynas, A. Sešek, and A. Švigelj, “A high performance room temperature THz sensor,” in *Proc. SPIE 9199, Terahertz Emitters, Receivers, and Applications V*, Sep. 2014, p. 91990K. doi: 10.1117/12.2060692.

[47] F. Simoens and J. Meilhan, “Terahertz real-time imaging uncooled array based on antenna- and cavity-coupled bolometers,” *Philosophical Transactions of the Royal Society A: Mathematical, Physical and Engineering Sciences*, vol. 372, no. 2012, p. 20130111, Mar. 2014, doi: 10.1098/rsta.2013.0111.

[48] J. Trontelj and A. Sešek, “Micro-machined millimeter wave sensor array for FM radar application,” in *Proc. SPIE 8544, Millimetre Wave and Terahertz Sensors and Technology V*, Oct. 2012, p. 85440G. doi: 10.1117/12.974706.

[49] D. T. Petkie *et al.*, “Active and passive imaging in the THz spectral region: phenomenology, dynamic range, modes, and illumination,” *Journal of the Optical Society of America B*, vol. 25, no. 9, p. 1523, Sep. 2008, doi: 10.1364/JOSAB.25.001523.

[50] K. B. Cooper, R. J. Dengler, N. Llombart, B. Thomas, G. Chattopadhyay, and P. H. Siegel, “THz Imaging Radar for Standoff Personnel Screening,” *IEEE Transactions on Terahertz Science and Technology*, vol. 1, no. 1, pp. 169–182, Sep. 2011, doi: 10.1109/TTHZ.2011.2159556.

[51] C. Daher *et al.*, “Room Temperature Direct and Heterodyne Detection of 0.28–0.69-THz Waves Based on GaN 2-DEG Unipolar Nanochannels,” *IEEE Transactions on Electron Devices*, vol. 63, no. 1, pp. 353–359, Jan. 2016, doi: 10.1109/TED.2015.2503987.

[52] M. Ferreras, D. Cibiraite-Lukenskiene, A. Lisauskas, J. Grajal, and V. Krozer, “Broadband Sensing Around 1 THz Via a Novel Biquad-Antenna-Coupled Low-NEP Detector in CMOS,” *IEEE Transactions on Terahertz Science and Technology*, vol. 11, no. 1, pp. 16–27, Jan. 2021, doi: 10.1109/TTHZ.2020.3031483.

[53] Z. Ahmad and K. K. O, “THz Detection Using p+/n-Well Diodes Fabricated in 45-nm CMOS,” *IEEE Electron Device Letters*, vol. 37, no. 7, pp. 823–826, Jul. 2016, doi: 10.1109/LED.2016.2573268.

[54] H. Qiao *et al.*, “Compact terahertz detector based on lightweight 3D-printed lens packaging,” *Electronics Letters*, vol. 55, no. 14, Jul. 2019, doi: 10.1049/el.2019.1446.

[55] J. Sun *et al.*, “Passive terahertz imaging detectors based on antenna-coupled high-electron-mobility transistors,” *Optics Express*, vol. 28, no. 4, p. 4911, Feb. 2020, doi: 10.1364/OE.385042.

[56] P. Hillger, J. Grzyb, R. Jain, and U. R. Pfeiffer, “Terahertz Imaging and Sensing Applications With Silicon-Based Technologies,” *IEEE Transactions on Terahertz Science and Technology*, vol. 9, no. 1, pp. 1–19, Jan. 2019, doi: 10.1109/TTHZ.2018.2884852.

[57] A. Golenkov, F. Sizov, and I. Lysiuk, “Frequency sensitive effect of rectifying FET terahertz detectors,” in *2016 46th European Microwave Conference (EuMC)*, Oct. 2016, pp. 1107–1110. doi: 10.1109/EuMC.2016.7824541.

[58] T. Shimizu, H. Moritsu, Y. Yasuoka, and K. Gamo, “Fabrication of Antenna-Coupled Microbolometers,” *Japanese Journal of Applied Physics*, vol. 34, pp. 6352–6357, Dec. 1995, doi: 10.1143/JJAP.34.6352.

[59] N. Hiromoto, A. Tiwari, M. Aoki, H. Satoh, M. Takeda, and H. Inokawa, “Room-temperature THz antenna-coupled microbolometer with a Joule-heating resistor at the center of a half-wave antenna,” in *2014 39th International Conference on Infrared, Millimeter, and Terahertz waves (IRMMW-THz)*, Sep. 2014, pp. 1–2. doi: 10.1109/IRMMW-THz.2014.6956173.

[60] X. Zheng *et al.*, “Enhancement of Real-Time THz Imaging System Based on 320 × 240 Uncooled Microbolometer Detector,” *Journal of Infrared, Millimeter, and Terahertz Waves*, vol. 37, no. 10, pp. 965–976, Oct. 2016, doi: 10.1007/s10762-016-0287-4.

[61] S. Bevilacqua and S. Cherednichenko, “Low noise nanometer scale room-temperature YBa2Cu3O7-x bolometers for THz direct detection,” *IEEE Transactions on Terahertz Science and Technology*, vol. 4, no. 6, pp. 653–660, Nov. 2014, doi: 10.1109/TTHZ.2014.2344435.

[62] P. Xiao *et al.*, “Planar double-slot antenna integrated into a Nb5N6 microbolometer THz detector,” *Optics Letters*, vol. 45, no. 10, p. 2894, May 2020, doi: 10.1364/ol.388771.

[63] M. Aoki, M. Takeda, and N. Hiromoto, “Electromagnetic Simulation for THz Antenna-Coupled Microbolometers Operated at Room Temperature,” *MAKARA Journal of Technology Series*, vol. 17, no. 1, Sep. 2013, doi: 10.7454/mst.v17i1.1919.

[64] A. Tiwari, H. Satoh, M. Aoki, M. Takeda, N. Hiromoto, and H. Inokawa, “Analysis of Microbolometer Characteristics for Antenna-Coupled Terahertz Detectors,” *Asian Journal of Chemicals*, vol. 25, pp. S358–S360, Mar. 2013, [Online]. Available: http://hdl.handle.net/10297/00026854

[65] A. Tiwari, H. Satoh, M. Aoki, M. Takeda, N. Hiromoto, and H. Inokawa, “THz Antenna-Coupled Microbolometer with 0.1-µm-wide Titanium Thermistor,” *International Journal of ChemTech Research*, vol. 7, no. 2, pp. 1019–1026, Feb. 2014, [Online]. Available: http://hdl.handle.net/10297/9268

[66] A. Banerjee, H. Satoh, D. Elamaran, Y. Sharma, N. Hiromoto, and H. Inokawa, “Performance improvement of on-chip integrable terahertz microbolometer arrays using nanoscale meander titanium thermistor,” *Journal of Applied Physics*, vol. 125, no. 21, Jun. 2019, doi: 10.1063/1.5083643.

[67] Q. Hu and P. L. Richards, “Design analysis of a high Tc superconducting microbolometer,” *Applied Physics Letters*, vol. 55, no. 23, pp. 2444–2446, Dec. 1989, doi: 10.1063/1.101998.

[68] Y. Shi, Y. Deng, P. Li, P. Fay, and L. Liu, “A 200 GHz Fully Integrated, Polarization-Resolved Quasi-Optical Detector Using Zero-Bias Heterostructure Backward Diodes,” *IEEE Microwave and Wireless Components Letters*, vol. 32, no. 7, pp. 891–894, 2022, doi: 10.1109/LMWC.2022.3155959.

[69] Ze Zhang, R. Rajavel, P. Deelman, and P. Fay, “Sub-Micron Area Heterojunction Backward Diode Millimeter-Wave Detectors With 0.18 pW/Hz^1/2 Noise Equivalent Power,” *IEEE Microwave and*

*Wireless Components Letters*, vol. 21, no. 5, pp. 267–269, May 2011, doi: 10.1109/LMWC.2011.2123878.

[70] P. Fay and Z. Zhang, "High-performance heterostructure backward diode detectors," in *Proc. SPIE 8031, Micro- and Nanotechnology Sensors, Systems, and Applications III*, May 2011, p. 80310B. doi: 10.1117/12.883677.

[71] S. M. Rahman, Z. Jiang, H. (Grace) Xing, P. Fay, and L. Liu, "Lens-coupled folded-dipole antennas for terahertz detection and imaging," *IET Microwaves, Antennas & Propagation*, vol. 9, no. 11, pp. 1213–1220, Aug. 2015, doi: 10.1049/iet-map.2014.0415.

[72] R. Lampe, "Design formulas for an asymmetric coplanar strip folded dipole," *IEEE Transactions on Antennas and Propagation*, vol. 33, no. 9, pp. 1028–1031, Sep. 1985, doi: 10.1109/TAP.1985.1143698.

[73] T. Endo, Y. Sunahara, S. Satoh, and T. Katagi, "Resonant frequency and radiation efficiency of meander line antennas," *Electronics and Communications in Japan (Part II: Electronics)*, vol. 83, no. 1, pp. 52–58, Jan. 2000, doi: 10.1002/(SICI)1520-6432(200001)83:1<52::AID-ECJB7>3.0.CO;2-7.

[74] A. Bandyopadhyay and A. Sengupta, "A Review of the Concept, Applications and Implementation Issues of Terahertz Spectral Imaging Technique," *IETE Technical Review*, vol. 39, no. 2, pp. 471–489, Jan. 2021, doi: 10.1080/02564602.2020.1865844.

[75] T. Nagatsuma, "Terahertz communications: Past, present and future," in *2015 40th International Conference on Infrared, Millimeter, and Terahertz waves (IRMMW-THz)*, Aug. 2015, pp. 1–2. doi: 10.1109/IRMMW-THz.2015.7327418.

[76] C. Dietlein, A. Luukanen, F. Meyer, Z. Popovic, and E. Grossman, "Phenomenology of passive broadband terahertz images," in *Proceedings of the 4th ESA Workshop on Millimetre-Wave Technology and Applications*, 2006, pp. 405–410.

*Chapter 2*

# SIMULATION OF HIGH-IMPEDANCE ANTENNA FOR THZ BOLOMETER

## 2.1 Impedance Matching Concept

Efficiency in the wireless communication system is highly correlated to the impedance matching between a radio wave generator to the transmitting device, such as antenna. Input impedance can be defined as: (i) the impedance presented by an antenna at its terminals, or (ii) the ratio of the voltage to current at a pair of terminals, or (iii) the ratio of the appropriate components of the electric to magnetic fields at a point. When an antenna with low input impedance, such as halfwave dipole antenna, is coupled to a high impedance device and applications, the power transfer to and from the antenna is poor due to the bad impedance matching.

Generally, efficiency of an antenna comprises of conduction efficiency, dielectric efficiency, and reflection (mismatch) efficiency. The conduction and dielectric losses of an antenna are difficult to be computed and separated each other. Usually they are measured as lumped together to form the conduction-dielectric efficiency. The conduction-dielectric efficiency ($e_{cd}$) can be defined as the ratio of the power delivered to the

radiation resistance $R_r$ to the total power delivered to radio and load resistance ($R_r$ + $R_L$). As for reflection efficiency can be described as dimensionless unit of the efficiency by considering the voltage reflection coefficient at the input terminals of the antenna.

In a transmitting antenna, from the total power that is supplied from the generator, half is dissipated as heat in the internal resistance of the generator. The other half is delivered to the antenna and then radiated, if a conjugate matching condition is fulfilled. Of the power delivered to the antenna, part is radiated through the mechanism provided by the radiation resistance and the other is dissipated as heat on the antenna material. A lossless and conjugate matched antenna will radiate half of the total power supplied by the generator by through radiation resistance mechanism, while the other half is dissipating as heat back in the generator. Analogous definition can be applied when talking antenna in receiving mode that half of the captured power transferred to the load and the other half power is scattered or re-radiated by the antenna material [1].

Some applications and devices in wireless communication system require a high-impedance characteristics antenna for the signals to be optimally radiated, such as photomixers. While for the detector based on electronic receiver, such as Schottky diodes and heterostructure backward

diodes (HBDs) have been reported having very high resistance operational [2]–[4]. Some other THz detectors have also been reported to have high resistance sensing element characteristics, such as VOx bolometer, MOSFET detector, and HEMT [5]–[7]. Potential impedance mismatch between devices and low-impedance half wavelength planar antennas resulting in the limited power coupling efficiency thus impact in relatively low detection performance. Impedance matching networks can be applied, but this will inevitably lead to the large size, complex systems and reduced detection bandwidth. To overcome these issues, high embedding impedance antennas are needed. As the resistance of a wire is proportional to its length, increasing the effective length will improve the characteristic impedance of the antenna.

## 2.2 Introduction to Folded Dipole Antenna

Among various planar type antenna, folded dipole antenna (FDA) has long been used for the high resistance application in photomixers as well as infrared detectors. FDA can be constructed by folding a λ/2 long element, that is basically a two-wire transmission line [8]. Since the FDA length can be considered as a λ-long loop antenna, the antenna is referred to as a folded loop, either open or closed. Thus, the real part of the FDA impedance can be adjusted by changing the width or the spacing between

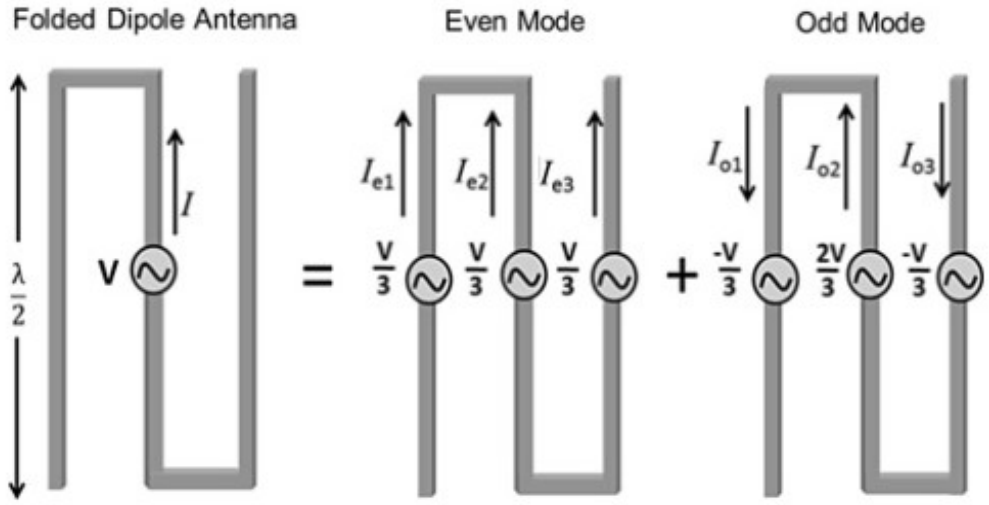


**Fig. 2-1 Decomposition of FDA into even-mode and odd-mode circuits for extraction of the radiating antenna currents [9].**

the antenna arms. One of the FDA analysis can be made by Even-Odd Mode (EOM) in which the current components decomposed into even- and odd-mode, as shown in Fig. 2-1 [9]. By decomposing the current components of the FDA, the single-port FDA with $N$ number of arms can be separated into even- and odd-mode of $N$-port networks. This approach permits the direct calculation of the embedding impedance and radiation patterns of the FDAs from the extracted mode currents. Once both current modes have been determined, the embedding impedance ($Z_{in}$) of the FDAs can be calculated from the current ratios and impedance matrix. Theoretically, $Z_{in}$ of an FDA is given by $Z_{in} = N^2 Z_0$, where $Z_0$ is the halfwave dipole antenna impedance [1].

In this chapter, we numerically study the FDA geometrical parameters to obtain the input impedance characteristics in transmitting mode and the antenna area efficiency in receiving mode for 1 THz operating frequency. As the heater resistance in THz antenna-coupled detectors can be enhanced almost freely by downscaling it to nano-scaled dimension, the FDA is designed with various geometries to attain high-impedance characteristics from several hundred to beyond 1 kΩ.

## 2.3 Simulation Conditions

The antenna is designed on a high-resistivity Si substrate, allow one to consider the FDA design for the real experiment based on the improvement prediction made by the presence of the substrate. In transmitting mode simulation, the resonant resistance is investigated with a source excitation on the antenna gap. While in receiving mode, area efficiency of FDA is determined from the power dissipation produced in the attached heater by the incident plane waves. An impedance matched condition is assumed by tuning the heater width so that its electrical resistance equals to the attained resonant resistance in the transmitting mode from the similar antenna design parameters. Within this antenna-heater design, a theoretical THz bolometer performance improvement in terms of the responsivity can be expected. This is because the detector

thermal resistance, which assumed to be proportional to electrical resistance of the heater part, plays a dominant role to generate temperature increase as a result from the incoming radiation. Therefore, the responsivity improvement could also be raised from the higher electrical resistance of the heater, in conjunction with its thermal counterpart. We introduce the figure of merit (FOM) from the product of antenna area efficiency and heater resistance which is equally designed to the resonant resistance of the antenna. Comparison is made to the low-impedance halfwave dipole antenna to assess the improvement made by the FDA. Time domain solver of the CST Studio Suite software is used for the numerical computation [10].

### 2.3.1 Design Modelling and Concept

The simulation model consists of a high-resistivity Si substrate, a vacuum airbox and antenna, as illustrated in Fig. 2-2. This model ensures the simulation domain include the high directivity performance through high resistivity substrate due to elimination of surface waves [11]–[13]. The real physical height of the substrate for fabrication is ~500 μm with the refraction index of 3.42. Within this height, the substrate can be modeled to behaves as a semi-infinite thick layer which about 4 times the effective wavelength at 1 THz. Therefore, we designed the wafer as a 20-

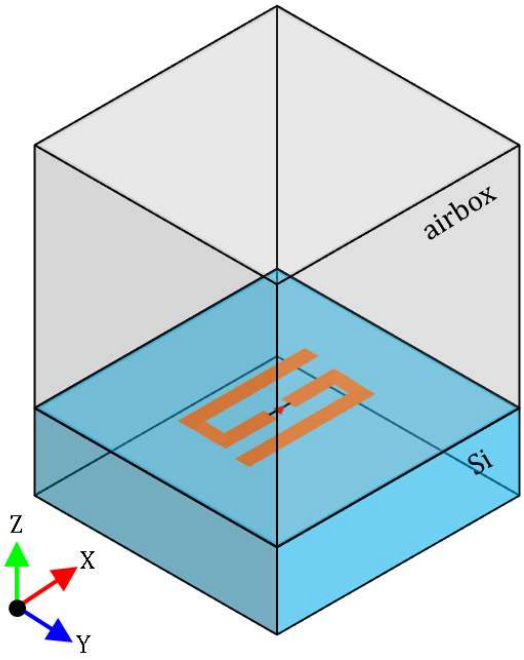


**Fig. 2-2 Simulation model in 3-dimensional volumetric structure comprising of high resistivity Si substrate, a vacuum airbox, and folded dipole antenna.**

μm thick Si box, backed by a perfectly matched layer (PML) boundary to form a semi-infinite substrate thickness. In addition, to accurately simulate the structure in a homogenous dielectric and to reduce the computational time, the background material was chosen with the same refractive index as the substrate box [14], [15]. The FDA geometries consist of antenna length ($l_a$), width ($w_a$), spacing between arms ($S$) and number of arms ($N$) defined as N=2(k-1)+1, with the fixed 11.5-μm gap ($g$) size as shown in Fig. 2-3a. The metallic antenna was designed from gold (Au) with the

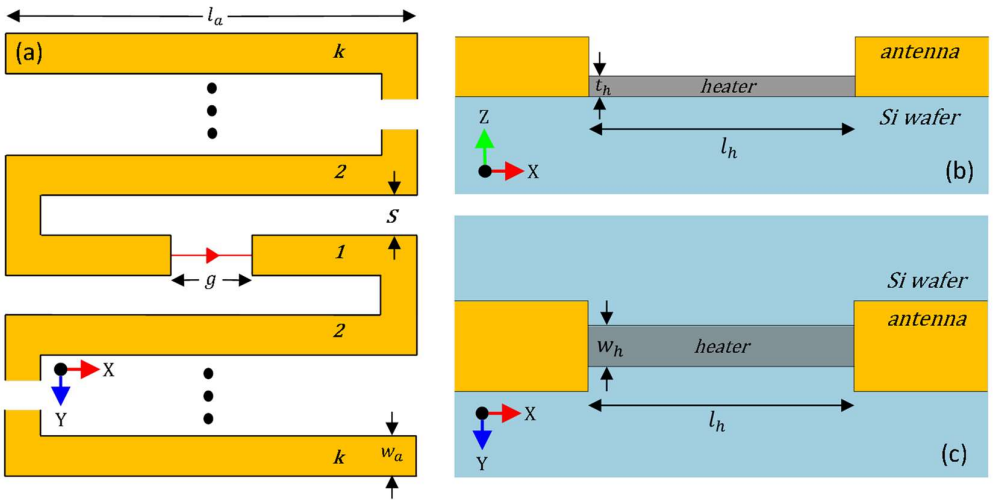


**Fig. 2-3 (a) 2-dimensional folded dipole antenna geometry parameters, (b) cross sectional view of the Ti heater and (c) top view of the Ti heater on the antenna gap.**

thickness of 200-nm which is larger than the skin-depth of the antenna material at 1 THz frequency. A 50-Ω discrete port is used at the antenna gap as the source excitation for transmitting mode simulation to extract the input impedance characteristics.

In the receiving mode simulation, a 1 V/m intensity of plane wave was launched from the substrate side towards $z+$ direction since the antenna on a thick dielectric substrate radiates preferentially into the dielectric half space. The polarization and electric field vector of the plane wave were set to be linear and parallel to the x-axis of the antenna,

respectively. A 50-nm thick metallic heater slab is placed at the antenna gap replacing the discrete port in transmitting mode to receive the induced displacement currents from the antenna, as illustrated in Fig. 2-3b and 2-3c. In order to keep the reciprocal input impedance behavior of the antenna in both transmitting and receiving mode, the length of the heater was kept the same as the antenna gap size ($l_h = g$). Furthermore, the heater width ($w_h$) was tuned according to the electrical resistance equal to the resonant resistance ($R_r$) of the antenna in the transmitting mode simulations, calculated as

$$w_h = \frac{\rho l_h}{R_r t_h}, \tag{2-1}$$

where $\rho$, $l_h$, and $t_h$ are the resistivity, length, and thickness of the Ti heater, respectively. Within this heater design, the impedance matched condition between antenna and heater can be hypothesized.

The simulation design and procedure of Folded Dipole Antenna is summarized in Fig. 2-4. Note that when designing the heater, a 50-nm heater thickness ($t_h$) is assumed and heater width ($W_h$) is set so that heater resistance is equals to the antenna resonant resistance ($R_r$) in a pure resistive material. The other detail of simulation parameters is given in table 2.1. The metal material conductivity is assumed room temperature value given in [16].

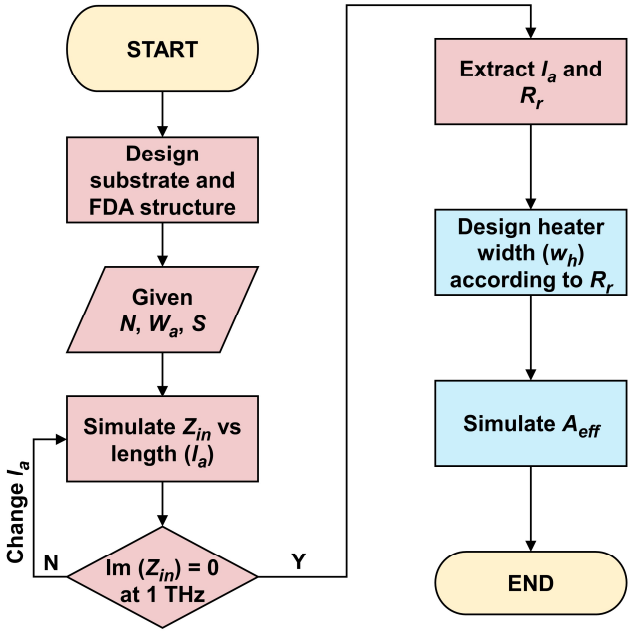


**Fig. 2-4 Simulation procedure for Folded Dipole Antenna design. Red and blue shaded processes are simulation in transmitting and receiving mode, respectively.**

**Table 2.1. Simulation parameter**

| | |
|---|---|
| **Target frequency** | 1 THz |
| **Antenna material** | Au ($\sigma = 4.4\times10^7$ S/m) |
| **Heater material** | Ti ($\sigma = 2.6\times10^6$ S/m) |
| **Thicknesses** | Antenna: 200 nm<br>Heater: 50 nm |
| **Heater length** | 11.5 μm |
| **Substrate material** | Silicon ($\rho$ = 1 kΩ.cm, $\varepsilon$ = 11.7) |

### 2.3.2 Simulation Setup

Both the simulation in transmitting and receiving modes were executed in the CST Studio Suite electromagnetic simulation software. Time domain solver was used based on the finite integration technique (FIT) in which the Maxwell's equation is discretized by its integral form. The model was discretized by using hexahedral meshing combined with perfect boundary approximation (PBA) to improve the geometry description with efficient memory compared to the standard finite differential time domain (FDTD) method [17]. In the global hexahedral mesh properties, the mesh size was determined by a maximum 15 cells per wavelength. To improve the accuracy in receiving mode, local mesh properties were applied to the heater element with 10 cells across the object structure in *x*-, *y*-, and *z*- directions. The perfectly matched layer (PML) absorbing boundary was defined at all the outer surfaces of the simulation model with the estimated reflection level of 1e-4. As a result, the total number of $1.5\times10^6$ and $3.5\times10^6$ mesh cells for transmitting and receiving mode simulation, respectively, were roughly generated. The computational server was equipped with 3 GHz Intel Xeon E5-2687W based CPU and 128 GB of memory. A "power flow" monitor was used in the receiving mode simulation to store the Poynting vectors of the electromagnetic field stimulated by the plane wave. So, the power dissipation into lossy

materials, such as Ti metal for the heater, can be extracted by integration of the Poynting vector over the enclosed surfaces.

## 2.4 Results

### *2.4.1 Transmitting Mode*

Parametric study of the FDAs was performed to analyze the effect of antenna geometries, such as length, width, and spacing to the input impedance characteristics with the fixed resonant frequency. As the FDA resonant frequency depends mainly on its length, we determine the resonant resistance ($R_r$) and resonant length ($L_r$) when the imaginary part crosses zero, as illustrated in Fig. 2-5. With the variation of length from $0.4\lambda_s$ to $0.7\lambda_s$, the reactive component of the impedance is changing from inductive to capacitive behavior. The resonant frequency is found near half wavelength of the antenna, indicates that the FDA has the first resonant length behavior analogous to a half-wave dipole antenna. Here the guiding wavelength ($\lambda_s$) defined as the effective wavelength at the interface between vacuum and Si substrate which calculated based on the effective permittivity ($\varepsilon_{eff}$). The equation used to calculate guiding wavelength is

$$\lambda_s = \frac{\lambda_0}{\sqrt{\varepsilon_{eff}}}, \tag{2-2}$$

and for effective permittivity ($\varepsilon_{eff}$) is given by

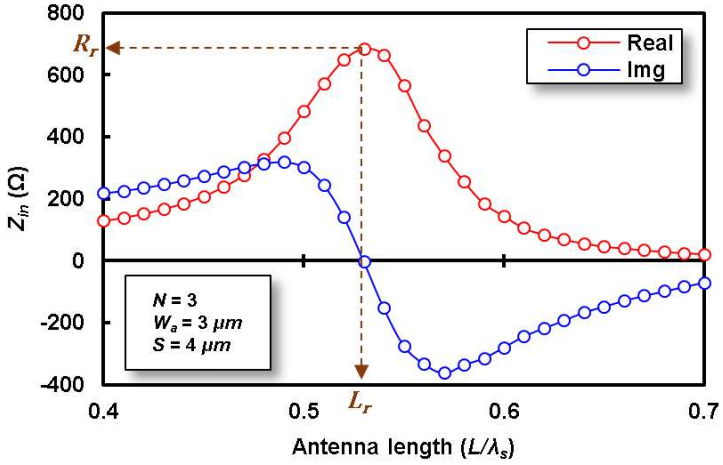


**Fig. 2-5 Resonant resistance ($R_r$) and length ($L_r$) extraction from the point where the imaginary part crosses zero.**

$$\varepsilon_{eff} = \frac{\varepsilon_s+1}{2}, \tag{2-3}$$

where $\lambda_0$ is the free space wavelength at resonant frequency and $\varepsilon_s$ is the permittivity of the Si substrate (11.7). The antenna with varied width and spacing were simulated ranging from 1- to 6-μm with 1-μm step. The $R_r$ and $L_r$ results were extracted from each width ($w_a$) and spacing ($S$) parameterization for 3-, 5- and 7-arm of FDA.

Fig. 2-6 shows the $L_r$ trend of FDA for all geometry variations. The resonant length is found around $0.5\lambda_s$ in all cases which comparable to the resonant length of the standard half-wave dipole antenna. The data points shown in the figure are fit to the linear fit line increasing to the antenna

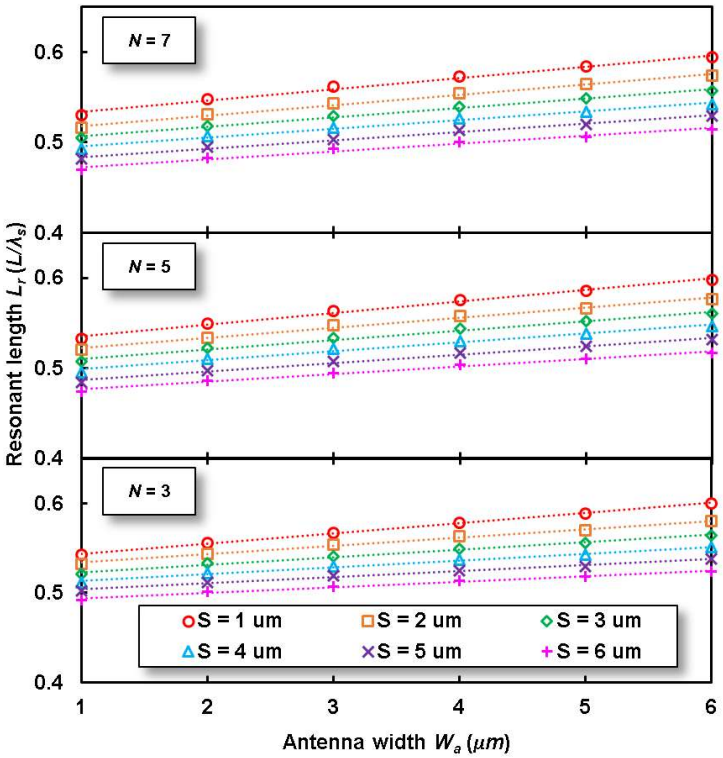


**Fig. 2-6 The resonant length ($L_r$) of FDAs as a function of antenna width for different spacing and number of arms.**

width for every spacing. The $L_r$ shows opposite trend to the antenna width and antenna spacing increment, where it is increasing to the former and decreasing to the latter. Yet this behavior is commonly different from the ordinary planar dipole antenna where the antenna length and width have opposite trend to the resonant frequency. This could be explained by the fact that the resonant frequency of planar meander antenna is changing as a function of the width to the spacing ratio for the fixed length, as reported in [18]. Hence the constant resonant frequency in this report affected to the

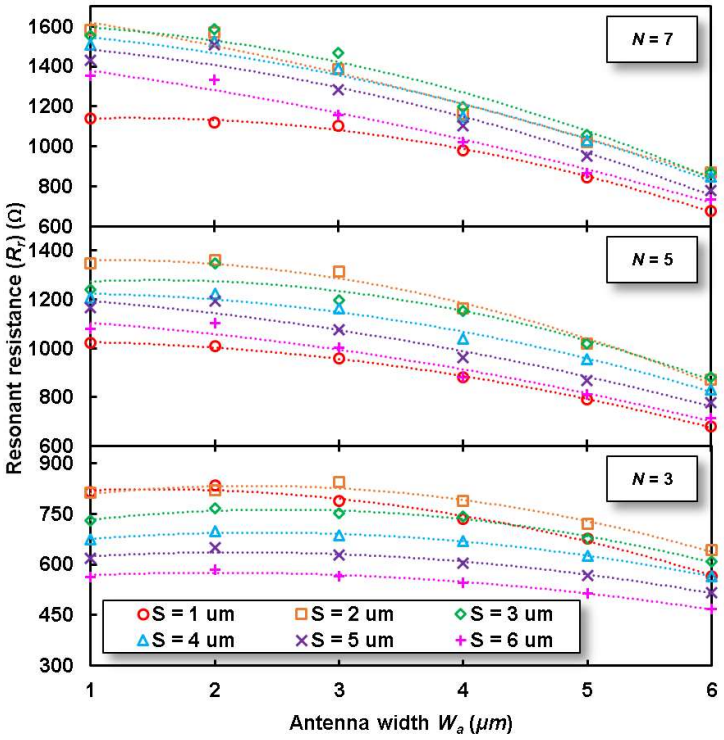


**Fig. 2-7 Resonant resistance ($R_r$) of FDAs as a function of antenna width for different spacing and number of arms.**

linear increase in the antenna resonant length to the width, but decreases to the spacing. The increasing number of arms has minor effect to the $L_r$ where the smaller number of arms has the longer $L_r$.

From each $L_r$, the correspond $R_r$ were obtained, as shown in Fig. 2-7. General trend of the $R_r$ is increasing with the number of arms and decreasing as the width becomes wider, which may be caused by the longer effective length and larger cross-sectional area, respectively. The $R_r$ of 3-

arm FDA is ranging from 450 Ω to 820 Ω for different width and spacing. However, there is a slight increase of $R_r$ from 1-μm to 3-μm width and then decreasing as the width becomes wider. While the increasing of spacing from 1-μm to 2-μm also shows resistance increase and further decreasing as the spacing wider. From the width and spacing variation, it shows a saturation point on the width and spacing around 2-μm. The identical behavior is found in the 5-arm and 7-arm of FDA, where the highest $R_r$ exceeds 1.3 kΩ and 1.5 kΩ, respectively. As the number of arms increases, the narrow spacing effect is found to be stronger where the saturation points of the $R_r$ is found in the wider spacing, i.e. 3-um in 7-arm FDA case. These results give a trade-off behavior between width and spacing to the FDA resonant resistances for different number of arms. The resistance decay in close proximity between FDA arms could be related to the strong electric field mutual coupling which cause interchange of the energy. Some of the energy radiated from FDA arms were received by the other arms and re-scattered in peculiar directions behaving as subsequent transmitters. In a very strong mutual coupling effect, the vector sum of radiated and re-scattered waves will influence the input impedance at the terminal and could complicates the analysis. In a practical manner, mutual coupling between FDA arms is difficult to predict but must be considered

due to its substantial contribution to the antenna impedance. Hence in this study we qualitatively predict the optimum proximity between FDA arms is changing as the number of arms increase. While in the narrow width case, the decaying resistance can be explained by the size effect caused from the mean free path of conduction electrons, which limits the electrical properties of a metal. A proper design is important when applying FDA in order to select desired resonant resistance for the impedance matching with the bolometer.

Another important result is the radiation efficiency which describe the capability of the antenna to converts the RF power accepted from the source terminal into dielectric or free-space radiation. It can be described as the ratio of the power delivered for the radiation resistance to the total power delivered including conduction loss caused by the antenna material property. Fig. 2-8 shows the radiation efficiency of FDA as a function of resonant resistance ($R_r$). The common trend in the radiation efficiency is increasing as the width increases for any given spacing and number of arms without any saturation point in width variety. As the $R_r$ higher, the efficiency becomes lower. This phenomenon may be attributed to high conduction (ohmic) loss as an effect of the skin depth in high frequency where the electrical current is flowing on the conductor surface instead of

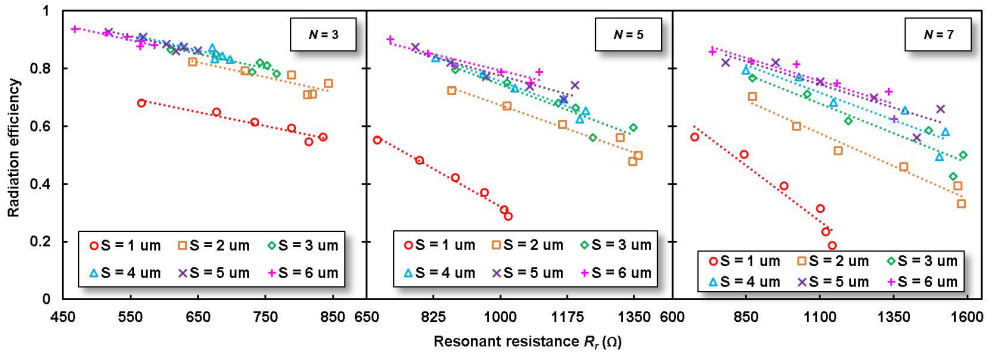


**Fig. 2-8 Radiation efficiency results of FDA as a function of resonant resistance from different spacing and number or arms.**

the full cross-sectional area. Hence the conductive heating loss on the antenna surface is increasing as the cross-sectional area decreases. As the $R_r$ comprises of radiation and loss resistance, the enhancement of ohmic loss affect to the reduction of radiation resistance, thus lower the radiation efficiency. Similar behavior occurs for each spacing in every number of FDA arms. However, FDA with larger spacing shows better radiation efficiency compared to smaller one, even with the same $R_r$. The efficiency has a large gap between 1-µm and 2-µm spacing, where the former efficiency drops significantly. This suggest the importance of spacing adjustment due to mutual coupling in between antenna arms that degrades the antenna efficiency performances. A higher number of FDA arms is desirable for high resistance performance, but with the consequence of decreasing radiation efficiency. Furthermore, a very large spacing offers

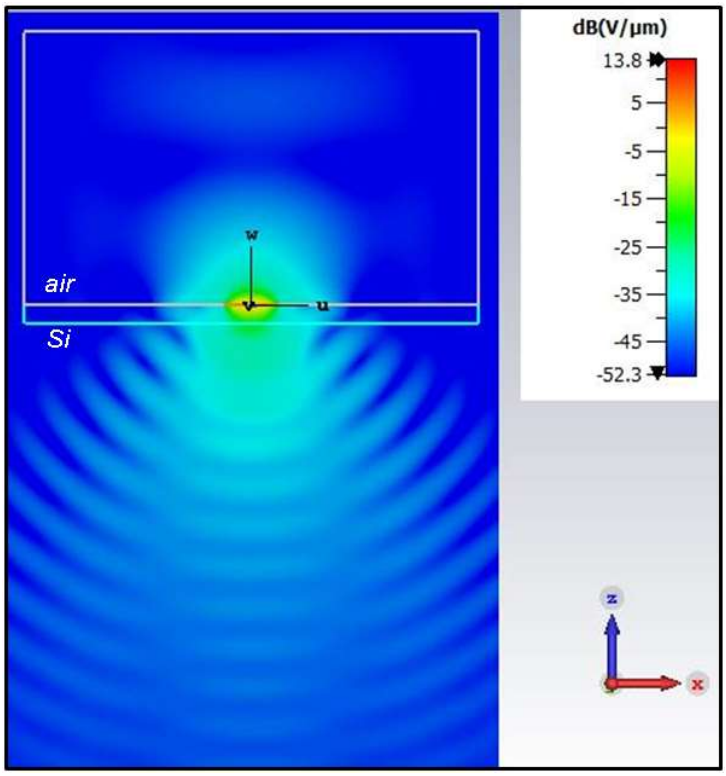


**Fig. 2-9 Electric field radiation characteristics of the semi-infinite substrate thickness shows the majority radiation towards the substrate direction.**

higher radiation efficiency, but it will impact to the larger pixel size which may increase the complexity during fabrication and measurement process of the bolometer.

The radiation characteristics of the FDA on semi-infinite Si substrate is displayed in Fig. 2-9. It shows the majority of the electromagnetic wave is emitted towards the Si substrate. As the antenna is located on the interface between two media with different dielectric constant, the radiated

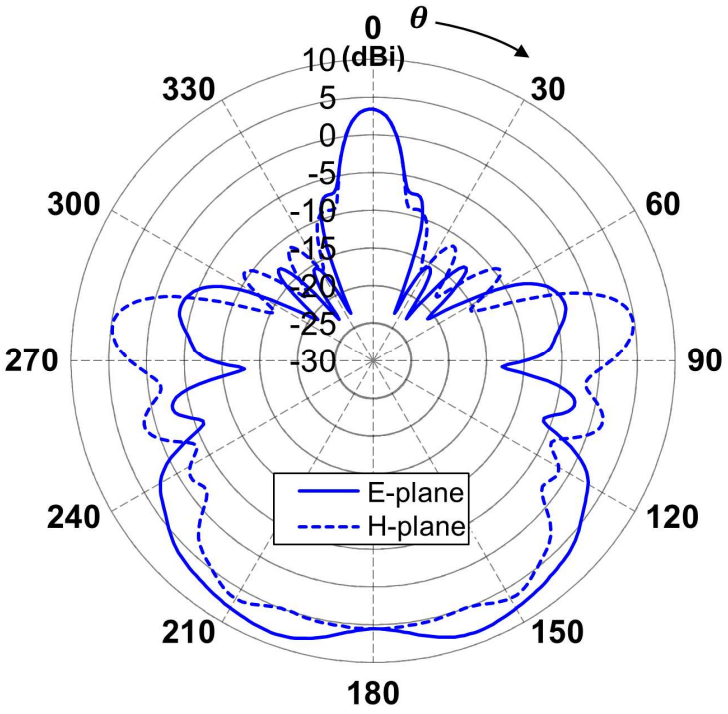


**Fig. 2-10 Simulated directivity pattern of the FDA.**

**The direction of θ = 180° correspond to the substrate**

power is proportional to $\varepsilon^{3/2}$, where $\varepsilon$ is the substrate to air permittivity ratio. In virtue of reciprocity theorem, for the antenna on a boundary between Si and air would receive power from the substrate-side approximately 40 times than that from the air-side [19]. However, some problem such as power loss to substrate modes may arise when substrate side illumination is utilized with a slab dielectric in real experiment. The pattern shown in Fig. 2-9 suggest the effectiveness of the semi-infinite thickness design to eliminate the substrate waves loss during simulation and it is suitable for the initial investigation of the antenna characteristics

[20]. Furthermore, the directivity pattern of FDA geometries follows the same tendency of substrate side radiation with some dependence on the antenna resistance that change the directivity value marginally. Fig. 2-10 shows the directivity pattern of the FDA in E- and H-plane at 1 THz for the 3-arms FDA. The simulated 1 THz directivity in the broadside (substrate) direction is 5.5 dBi. The use of high-resistivity Si substrate allows the majority of the electromagnetic wave emitted to the substrate direction ($\theta$ = 180°). The pattern can be explained by the ratio $\varepsilon^{3/2}$ of powers radiated to the substrate and air side, where ε is the permittivity of the substrate [21]. This pattern is important considering the incident wave for the THz detector will be from the substrate direction where the higher gain is expected. An array configuration is also appropriate to improve the antenna gain. However, for THz imaging applications, the array configuration is mainly applied to acquire 2D image in a parallel manner, and the interaction between antennas needs to be. Therefore, our target in this study is to design and simulate a single pixel THz antenna, as the same assumption will be applied during the experimental procedure in the next chapter.

### *2.4.2 Receiving Mode*

In the receiving mode simulation, a heater was placed at the antenna gap replacing the source excitation in the transmitting mode. The heater was designed to match the resistance obtained in transmitting mode, as explained in previous sub-section. The incoming radiation source is a 1 V/m EM wave from the substrate side towards $z+$ direction. Therefore, the incident power density ($W_i$) has the uniform intensity that can be calculated by

$$W_i = \frac{E^2}{2\eta_s}, \tag{2-4}$$

where $\eta_s$ is the wave impedance of the substrate material. Note that the free-space characteristic impedance needs to be considered due to the antenna presence at the boundary interface. The time-average power dissipation ($P_r$) in the heater structure was numerically calculated based on the integration of the Poynting vectors over the heater surfaces, expressed as

$$P_r = \frac{1}{2}\int_A Re(E \times H^*)dA, \tag{2-5}$$

where $E$ and $H$ is the electric and magnetic field intensity, respectively. Based on equation (2-4) and (2-5), the power capturing characteristics of the antenna can be calculated as the effective area ($A_e$) by

$$A_e = \frac{P_r}{W_i}, \tag{2-6}$$

with the $P_r$ and $W_i$ represented in Watt and W/m$^2$, respectively. The effective area of the receiving antenna can be further extended to the antenna area efficiency ($A_{eff}$) described as the ratio of effective area to the physical area ($A_p$) [22],

$$A_{eff} = \frac{A_e}{A_p}. \tag{2-7}$$

Here we assume the square of the effective wavelength (${\lambda_s}^2$) as the $A_p$. For FDA and half-wave dipole antenna, the effective area is typically smaller than the physical area of ${\lambda_s}^2$ due to the limited antenna gain.

Fig. 2-11 shows the antenna area efficiency ($A_{eff}$) of FDAs as a function of width for different spacing and number of arms. In general, the $A_{eff}$ is decreasing as the number of FDA arms increases, which is similar to the radiation efficiency results in Fig. 2-7 as the effect of higher resonant resistance. However, the $A_{eff}$ changes over width and spacing becomes

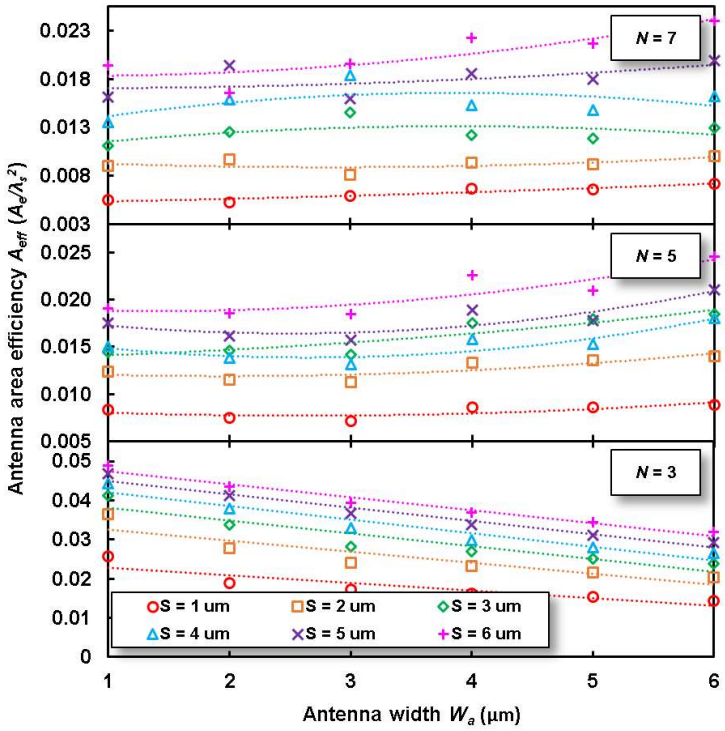


**Fig. 2-11 Antenna area efficiency as a function of antenna width for different spacing and number or arms.**

different as the number of arm increases. For the 3-arm FDA, the $A_{eff}$ is slightly decrease as the antenna width wider. It shows opposite trend with the radiation efficiency in transmitting mode where the narrow width antenna (higher resistance) has lower radiation efficiency. While in the 5- and 7-arm FDA, where the resistance is higher, the $A_{eff}$ shows nearly constant result with the antenna width increment. As for arm spacing effect, the $A_{eff}$ is increasing with the spacing regardless the number of arms. The

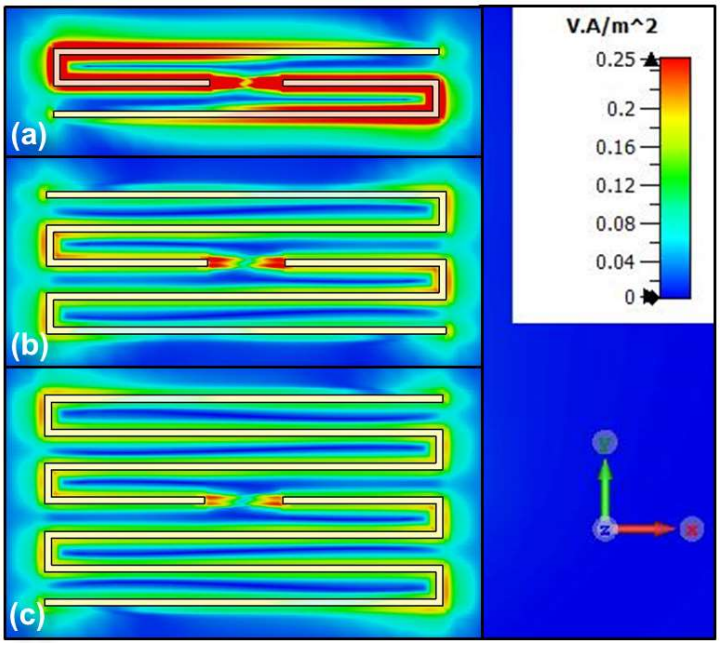


**Fig. 2-12 Power loss distribution of FDA in different antenna arms: (a) N = 3, (b) N = 5, and (c) N = 7.**

highest $A_{eff}$ is about 5 percent in the 3-arm FDA with 1-μm width and 6-μm arm spacing.

Fig. 2-12 shows the power loss distribution in the antenna-coupled microbolometer surface for the antenna width of 1-μm and spacing of 4-μm viewing from the top side. It is clearly seen that the power losses are distributed almost equally in entire antenna surface and central heater area. As the number of arms increase, the average induced power loss is decreases due to larger antenna surface area. This means the total power density on the antenna structure is higher compared to the one absorbed into heater. Typically, the power loss on antenna surface does not

contribute to the overall antenna-coupled microbolometer performance. The reason is that in the fabricated device only the heater part is suspended on top of the air gap hole, while the rest of antenna slab remains on the substrate surface. Hence the temperature increase in the bolometer is mainly depends on the power loss of the heater itself, while power loss in the antenna has insignificant effect.

Commonly, the area efficiency of FDA is lower compared to the half-wave dipole antenna, with the maxima close to 5 percent according to Fig. 2-11. However, the responsivity improvement in THz bolometer could also be expected from the higher heater electrical resistance, even with lower power efficiency caused by conduction loss in the high-impedance antenna. The bolometer responsivity is defined as the ratio of the electrical output signal of the bolometer to the input radiation power, with the unit of volts per watt (V/W) or amperes per watt (A/W) if the output signal current is measured. When an incident radiation is travels toward bolometer surface, the power is absorbed and cause a temperature increase. According to the heat transfer equation, the output signal voltage ($V_S$) appeared at the bolometer is proportional to [23]

$$V_S \propto \frac{\alpha A_D P_o}{G}, \tag{2-8}$$

where $\alpha$ is the temperature coefficient of resistance (TCR) of the bolometer material, $A_D$ is the detector effective area, $P_o$ is the incident power density, and $G$ is the effective thermal conductance of the bolometer. In the presence of an antenna as an absorbing component, the detector area could be replaced by the effective area ($A_e$) of the antenna. A large effective area is preferred to couple more power to the bolometer hence increase the output signal. The other way to increase the responsivity is by reducing the overall thermal conductance of the bolometer by downscaling it. Since the bolometer thermal resistance becomes larger, the antenna should sufficiently enlarge its resistance for the impedance matching between the two. However, the typical high impedance antenna has lower efficiency due to larger ohmic losses in the antenna surfaces, therefore the overall bolometer performance can be explained by the multiplication of the antenna effective area and bolometer resistance as the figure of merit defined as

$$FOM = A_{eff} \times R_h. \tag{2-9}$$

A higher FOM is proportional to the higher responsivity in the THz antenna-coupled bolometer. Fig. 2-13 shows the calculated FOM of various FDA geometries, taken from the product of antenna area efficiency ($A_{eff}$) and heater resistance which equals to the resonant resistance ($R_r$)

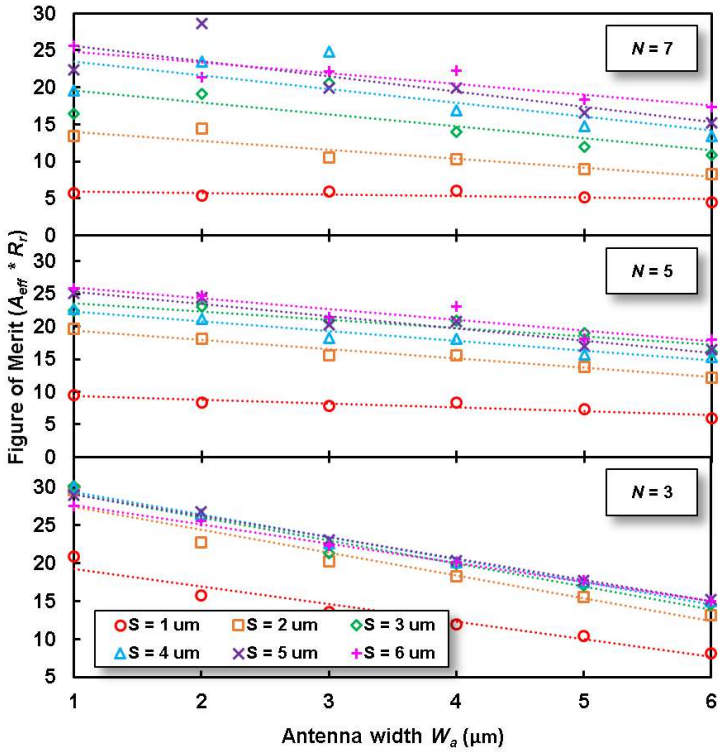


**Fig. 2-13 The figure of merit (FOM) as a result of antenna area efficiency and heater resistance.**

of the antenna based on equation (2-1). It is clear that 3-arm FDA has largest FOM compared to the 5- and 7-arm FDA. The optimum FOM is 30 in the 3-arm FDA for 1-μm wide and 4-μm arm spacing. FDA with higher number or arm shows a comparable pattern of FOM, but with rather constant effect to the antenna width. The FOM is increasing with the spacing and shows higher saturation point as the number of arms increase. These results reveal that the improvement of the antenna-coupled microbolometer could be attained with the folded dipole antenna and high resistance heater. However, a trade-off between resistance and efficiency

performance must be considered to obtain the optimum condition. To justify the responsivity improvement being made by high impedance antenna and heater, a comparison to half-wave dipole antenna is taken. We have designed a half-wave dipole antenna with 45-μm long, 3-μm wide, and simulated it with the identical simulation condition and material properties as used in the FDA design simulation. A low input impedance characteristics of 23 Ω was obtained. The heater thickness was 200-nm and used to determine the heater width to form an impedance matched condition. The area efficiency of half-wave dipole antenna is found to be 8.3 percent with the FOM of 2.1. The FOM result comparison between FDA and half-wave dipole antenna reveals the improvement by a factor of 13.5 can be expected from the implementation of FDA. Note that this performance increase assumption is based on the heater electrical resistance which dominates the thermal resistance of the entire bolometer structure, thus the responsivity could be enhanced linearly based on the heater electrical resistance increase. However, the improvement factor could have different result if the comparison is made with different type of antenna used for antenna-coupled detectors, such as bowtie, spiral and log-periodic antennas with various efficiency, impedance, or bandwidth performances [24]. In this study, we intended the detector improvement with respect to the higher resistance heater, thus the FDA is chosen among

many types of antenna due to its high-impedance characteristics. However, the comparison to the half-wave dipole antenna result is considered because it is the most commonly used planar antenna type for antenna-coupled microbolometer [25].

## 2.5 Conclusion

In this chapter, folded dipole antennas (FDA) has been designed and simulated with various geometries at 1 THz frequency. The FDA could yield high input impedance characteristics up to 1.5kΩ with the proper selection of antenna dimension. Simulation in receiving mode reveals that the responsivity improvement in THz bolometer could be attained from the product of antenna area efficiency and resonant resistance. Optimum performance is obtained from the 3-arm FDA with 1-μm wide and 4-μm arm spacing. A comparison with half-wave dipole antenna is made to justify the improvement made with FDA, based on the assumption that heater resistance is dominating the thermal resistance of entire detector and responsivity is proportional to the heater resistance increase. This assumption needs to be verified by device fabrication with high heater resistances. Lastly, the result presented in this chapter could be used as the starting point in the realization of high-impedance antenna-coupled microbolometer in the next chapter.

## References


[1] C. Balanis, “Antenna Theory: Analysis and Design,” in *Antenna Theory: Analysis and Design*, 4th ed., Hoboken, New Jersey: Wiley, 2016, pp. 75–78.

[2] Y. Shi, Y. Deng, P. Li, P. Fay, and L. Liu, “A 200 GHz Fully Integrated, Polarization-Resolved Quasi-Optical Detector Using Zero-Bias Heterostructure Backward Diodes,” *IEEE Microwave and Wireless Components Letters*, vol. 32, no. 7, pp. 891–894, Jul. 2022, doi: 10.1109/LMWC.2022.3155959.

[3] Ze Zhang, R. Rajavel, P. Deelman, and P. Fay, “Sub-Micron Area Heterojunction Backward Diode Millimeter-Wave Detectors With 0.18 pW/Hz$^{1/2}$ Noise Equivalent Power,” *IEEE Microwave and Wireless Components Letters*, vol. 21, no. 5, pp. 267–269, May 2011, doi: 10.1109/LMWC.2011.2123878.

[4] P. Fay and Z. Zhang, “High-performance heterostructure backward diode detectors,” in *Proc. SPIE 8031, Micro- and Nanotechnology Sensors, Systems, and Applications III*, May 2011, p. 80310B. doi: 10.1117/12.883677.

[5] I. E. Carranza, J. Grant, J. Gough, and D. R. S. Cumming, “Metamaterial-Based Terahertz Imaging,” *IEEE Transactions on Terahertz Science and Technology*, vol. 5, no. 6, pp. 892–901, Nov. 2015, doi: 10.1109/TTHZ.2015.2463673.

[6] M. I. W. Khan, S. Kim, D.-W. Park, H.-J. Kim, S.-K. Han, and S.-G. Lee, “Nonlinear Analysis of Nonresonant THz Response of MOSFET and Implementation of a High-Responsivity Cross-Coupled THz Detector,” *IEEE Transactions on Terahertz Science and Technology*, vol. 8, no. 1, pp. 108–120, Jan. 2018, doi: 10.1109/TTHZ.2017.2778499.

[7] H. Hou, Z. Liu, J. Teng, T. Palacios, and S.-J. Chua, “A sub-terahertz broadband detector based on a GaN high-electron-mobility transistor with nanoantennas,” *Applied Physics Express*, vol. 10, no. 1, p. 014101, Jan. 2017, doi: 10.7567/APEX.10.014101.

[8] R. Lampe, “Design formulas for an asymmetric coplanar strip folded dipole,” *IEEE Transactions on Antennas and Propagation*, vol. 33, no. 9, pp. 1028–1031, Sep. 1985, doi: 10.1109/TAP.1985.1143698.

[9] S. M. Rahman *et al.*, “Lens-coupled folded-dipole antennas for terahertz detection and imaging,” *IET Microwaves, Antennas & Propagation*, vol. 9, no. 11, pp. 1213–1220, Aug. 2015, doi: 10.1049/iet-map.2014.0415.

[10] “CST Studio Suite.” 3DS Simulia. [Online]. Available: https://www.3ds.com/products-services/simulia/

[11] G. P. Szakmany, A. O. Orlov, G. H. Bernstein, M. Lin, and W. Porod, “Multiphysics THz Antenna Simulations,” *IEEE Journal on Multiscale and Multiphysics Computational Techniques*, vol. 3, pp. 289-294, 2018, doi: 10.1109/JMMCT.2018.2886567.

[12] D.-T. Nguyen *et al.*, “Broadband THz Uncooled Antenna-Coupled Microbolometer Array—Electromagnetic Design, Simulations and Measurements,” *IEEE Transactions on Terahertz Science and Technology*, vol. 2, no. 3, pp. 299-305, May 2012, doi: 10.1109/TTHZ.2012.2188395.

[13] N. Llombart and A. Neto, “THz Time-Domain Sensing: The Antenna Dispersion Problem and a Possible Solution,” *IEEE Transactions on Terahertz Science and Technology*, vol. 2, no. 4, pp. 416-423, Jul. 2012, doi: 10.1109/TTHZ.2012.2197949.

[14] J. Montero-de-Paz, E. Ugarte-Munoz, L. E. Garcia-Munoz, I. Camara Mayorga, and D. Segovia-Vargas, “Meander Dipole Antenna to Increase CW THz Photomixing Emitted Power,” *IEEE Transactions on Antennas and Propagation*, vol. 62, no. 9, pp. 4868-4872, Sep. 2014, doi: 10.1109/TAP.2014.2346708.

[15] N. Llombart and A. Neto, “Authors’ Reply,” *IEEE Transactions on Terahertz Science and Technology*, vol. 4, no. 1, Jan. 2014, doi: 10.1109/TTHZ.2013.2294401.

[16] W. M. Haynes, D. R. Lide, and T. J. Bruno, *CRC Handbook of Chemistry and Physics 97 th Edition*, 97th ed. Boca Raton: CRC Press, 2016.

[17] T. Weiland, M. Timm, and I. Munteanu, “A practical guide to 3-D simulation,” *IEEE Microwave Magazine*, vol. 9, no. 6, pp. 62-75, Dec. 2008, doi: 10.1109/MMM.2008.929772.

[18] T. Endo *et al.*, “Resonant frequency and radiation efficiency of meander line antennas,” *Electronics and Communications in Japan (Part II: Electronics)*, vol. 83, no. 1, pp. 52–58, Jan. 2000, doi: 10.1002/(SICI)1520-6432(200001)83:1<52::AID-ECJB7>3.0.CO;2-7.

[19] B. A. Lail *et al.*, “Infrared dipole-coupled bolometer response on a hemispherical silicon immersion lens,” *Infrared Physics & Technology*, vol. 52, no. 2–3, pp. 89-96, Mar. 2009, doi: 10.1016/j.infrared.2009.03.001.

[20] T. K. Nguyen and I. Park, “Comparative study of strip line dipole antenna on semi-infinite and lens substrates at terahertz frequency,” in *The 8th European Conference on Antennas and Propagation*, Apr. 2014, pp. 2470-2474. doi: 10.1109/EuCAP.2014.6902319.

[21] M. Kominami, D. Pozar, and D. Schaubert, “Dipole and slot elements and arrays on semi-infinite substrates,” *IEEE Transactions on Antennas and Propagation*, vol. 33, no. 6, pp. 600–607, Jun. 1985, doi: 10.1109/TAP.1985.1143638.

[22] T. Morf *et al.*, “Wide bandwidth room-temperature THz imaging array based on antenna-coupled MOSFET bolometer,” *Sensors and Actuators A: Physical*, vol. 215, pp. 96-104, Aug. 2014, doi: 10.1016/j.sna.2014.03.019.

[23] P. W. Kruse, *Uncooled Thermal Imaging Arrays, Systems, and Applications*. Bellingham, USA: SPIE Press, 2001.

[24] F. J. González and G. D. Boreman, “Comparison of dipole, bowtie, spiral and log-periodic IR antennas,” *Infrared Phys. & Tech.*, vol. 46, no. 5, pp. 418-428 Jun. 2005, doi: 10.1016/j.infrared.2004.09.002.

[25] N. Hiromoto *et al.*, “Room-Temperature Terahertz Antenna-Coupled Microbolometers with Titanium Thermistor and Heater,” in *2019 16th International Conference on Quality in Research (QIR)*, Jul. 2019, pp. 1-5. doi: 10.1109/QIR.2019.8898200.

# *Chapter 3*

# FABRICATION AND MEASUREMENT OF TERAHERTZ BOLOMETER WITH HIGH-IMPEDANCE ANTENNA

## 3.1 Introduction

Typical modern bolometer arrays consist of a pixel structure that firstly developed by Honeywell, Inc. It is called a monolithic structure and made by Si micromachining fabrication technique. The detecting area constructed from a thin membrane made of $Si_3N_4$ and a thin film deposited on top of it for sensing element. Initial material used for the thin film was a semiconductor made of vanadium oxide ($VO_x$) [1]. The recent advances in micro electro mechanical systems (MEMS) technology employed sensitive thermal bolometric detectors on thermally isolated hanging membranes. The thermally sensitive layer that changes its sheet resistance according to the change of the temperature has been developed using various materials such as metals and semiconductors.

Modern bolometers consist of separated absorber and the temperature sensor. Heater temperature is increase due to the absorption of electromagnetic radiation which in turn causes the change in the thermistor temperature and resistance [2]. For the longer wavelength ($\lambda$) in the far-IR

and THz region, the absorber size should be proportional to λ due to the diffraction limit in focusing the incoming light [3]. The larger absorber and temperature sensor, the more difficult it is to realize the low thermal conductance ($k$) and low heat capacity ($C_p$) characteristics. Antenna-coupled bolometer was then introduced to solve this issue, where the incoming THz radiation detected by the antenna and transferred to the bolometer. Antenna-coupled bolometers have been studied extensively since early 80's where the radiation is absorbed by an antenna and converted to heat by the load resistor or heater [4]. The sensitivity of a bolometer defined as the output signal (voltage or current) with respect to the input radiant power falling on the pixel element. It could potentially be enhanced by using a novel structure such as integrated thermistor and heater which are electrically separated but thermally coupled [5], [6]. Within this structure, individual optimization of heater and thermistor resistance is possible for the sensitivity enhancement.

Heater resistance design is important to match the impedance of the coupled antenna for the optimum power transfers as the induced current at the antenna gap flows into the heater. The electromagnetic simulation of the antenna-coupled bolometer demonstrates the performance improvement can be expected for the heater with optimum resistance [7].

As for thermistor, the most important parameter is the temperature coefficient of resistance (TCR), because the responsivity ($R_v$) and noise equivalent power (NEP) is proportional and inversely proportional to the TCR, respectively.

Commonly used thermistor materials are semiconductors made of amorphous silicon (a-Si), Vanadium oxide ($VO_x$), and metal-based material such as Bismuth (Bi), Platinum (Pt) and Titanium (Ti). The main benefit of metallic bolometer is the low noise which mainly dominated by the shot and the thermal noise. Therefore, the device performance can be improved by the selection of metal with the high TCR which is difficult to obtained in semiconductor-based materials such as a-Si and $VO_x$. In this study, Ti is selected as the material for thermistor and heater due to its low electrical and thermal conductivities, immunity to electromigration, low flicker noise, and compatible with the Si wafer processing technology [8]–[10].

The electrical responsivity of meander shape thermistor has been investigated to be twice larger than that of the straight wires due to four-time larger electrical resistance [11]. The scaling trend of the Ti bolometer is also verified the cut-off frequency ($f_c$) improvement and decrease of $R_v$ if the length was reduced while keeping the same width and thickness in

both heater and thermistor [11]. This trade-off was partially relaxed with the use of meander shape thermistors where effective length can be improved.

The size effects have been investigated in the narrow width Ti line with reduced TCR of one third than that of bulk material [12]. The TCR of the thermistor also gets affected by the presence of defects or grain boundaries, and can be improved by annealing. Performance improvement of bolometer by Joule heating effect has also been conducted [13].

Further scaling study reveals the importance of the uniform resistance increase in thermistor and heater. The resistance increase will further reduce the thermal conductance of the bolometer, if the heat loss mechanism is dominated by the heater. Thermistor resistance was increased by using meander structure. As for heater, resistance can be increased by the reduction in width or thickness. Increasing heater resistance will lead to the enhanced responsivity and reduction of NEP, because the noise source is dominated by thermal noise in the thermistor. However, heater resistance increase requires a drastic change in the antenna. Halfwave dipole antenna that commonly used in a THz detector has relatively low impedance characteristics, and can only be optimally coupled with a low resistance heater. Therefore, heater resistance

improvement should be followed by the development of the antenna with higher impedance at the same resonant frequency. Folded dipole antenna (FDA) has been discussed and proposed as the solution in the previous chapters.

In this chapter, we discuss the design and fabrication of the antenna-coupled microbolometer with varied Ti heater width to improve heater resistance. A common 0.1-μm-wide meander thermistor was used. Electrical-based experiments were performed to extract the electrical resistance, TCR, thermal resistance, noise and electrical responsivity. Optical-based experiments were performed to evaluate THz responsivity at 1 THz frequency with two antenna types of halfwave and folded dipole.

## 3.2 Device Concept of Ti Microbolometers

Fig. 3-1 shows the fabricated antenna-coupled bolometer structure. Stacked heater and thermistor located at the center of a half wave and folded dipole antenna designed for 1 THz detection. Thermistor is electrically separated from the heater by 100-nm-thick $SiO_2$ interlayer, but thermally coupled each other. Cavity was formed to detach the heater-thermistor stack from the silicon (Si) substrate, for large thermal isolation and temperature rise. Two set of samples were fabricated with the variation in 0.1 and 0.2 μm heater thicknesses. The detector samples packaged on a

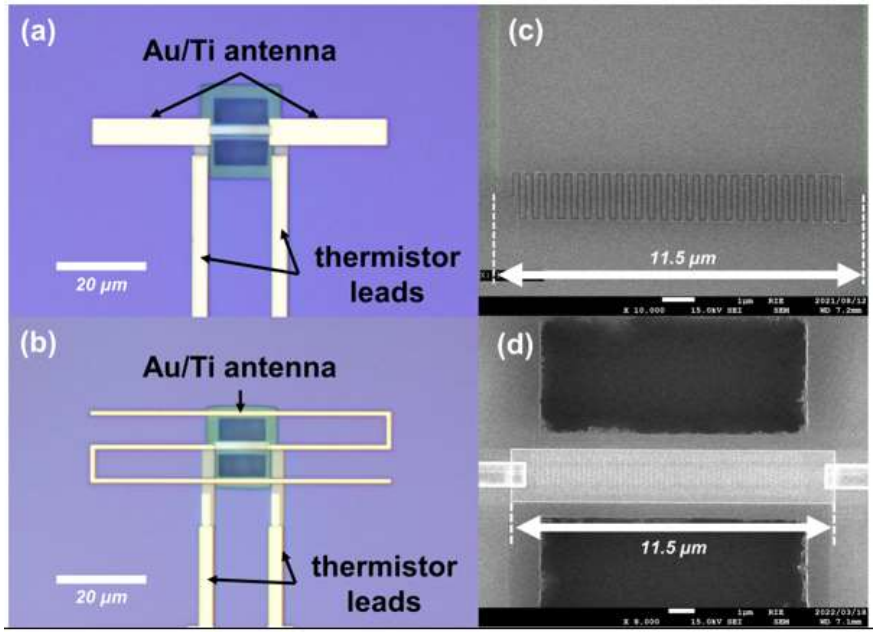


**Fig. 3-1 OM and FESEM images of the antenna-coupled detector: (a) Detector with halfwave dipole antenna; (b) Detector with folded dipole antenna; (c) Fabricated meander thermistor on $SiO_2$ interlayer with effective length of 89.5 μm; (d) Suspended heater and thermistor devices above cavity hole for detector's thermal isolation from the Si substrate.**

6 mm x 6 mm chip and wire bonded through the measurement pads for THz optical characterization. While the identical detector samples but without the antenna were also prepared for material parameter and electrical characterization. Fig. 3-1a and 3-1b show the structural observation based on optical microscope (OM) for the fabricated detector

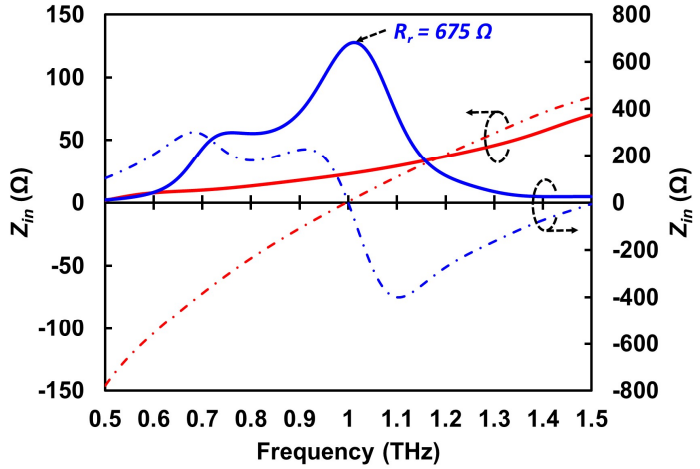


**Fig. 3-2 Complex impedance characteristics of the folded (blue line) and halfwave (red) dipole antenna. Solid line represents real impedance, while dashed line represent imaginary impedance for the antenna length and width shown in Table 3.1**

coupled to halfwave and folded dipole antenna, respectively. Fig. 3-1c and 3-1d show the field-emission scanning electron microscope (FE-SEM) observation of meander thermistor and suspended heater-thermistor structure above the cavity hole, respectively. In this study, a common 0.1 μm wide thermistor was designed in meander structure for longer effective length and higher resistance. The heater was designed in fixed length ($L_{hea}$) with twelve different widths ($W_h$). A 11.5 μm-long heater was considered due to the gap size between antenna arms where the 1 THz resonant frequency is attained. As we fabricated a wide range of heater resistances,

two type of antenna in the shape of halfwave and folded dipole were designed and fabricated with individual antenna length ($L_{ant}$) and width ($W_{ant}$). Note that both antennas have a resonant frequency of 1 THz from the electromagnetic simulation to effectively transfer the incident THz waves to low and high heater resistances, as shown by their complex impedance characteristic plot in Figure 3-2 [14]. Table 3.1 summarizes the structure dimension of thermistor, heater, and antennas.

**Table 3.1 Device parameters and dimensions**

| Device | Material | Dimensions (μm) | | |
|---|---|---|---|---|
| | | Length | Width | Thickness |
| Thermistor | Ti | 89.5 | 0.1 | 0.05 |
| Heater | Ti | 11.5 ($L_h$) | 0.1 - 2.1 ($W_h$) | 0.1, 0.2 |
| Halfwave dipole | Au/Ti | 52 ($L_{ant}$) | 5.2 | 0.2/0.02 |
| Folded dipole | Au/Ti | 61 ($L_{ant}$) | 1 | 0.2/0.02 |

## 3.3 Fabrication Process

The studied detector is composed of integrated titanium (Ti) thermistor, interlayer, Ti heater, and gold (Au) antenna stacked on a high resistivity Si substrate (p-type, ρ:4.2-9.5 kΩ.cm). Fabrication processes were performed sequentially from the bottom to top layer. Prior to thermistor fabrication, 200-nm-thick thermal oxide (TO) SiO2 was grown on the Si substrate using the wet oxidation technique under atmospheric pressure for 30 min at 1000 ◦C, without any pre- and post-treatment. After that, meander thermistor was patterned and then deposited. Fig. 3-3a

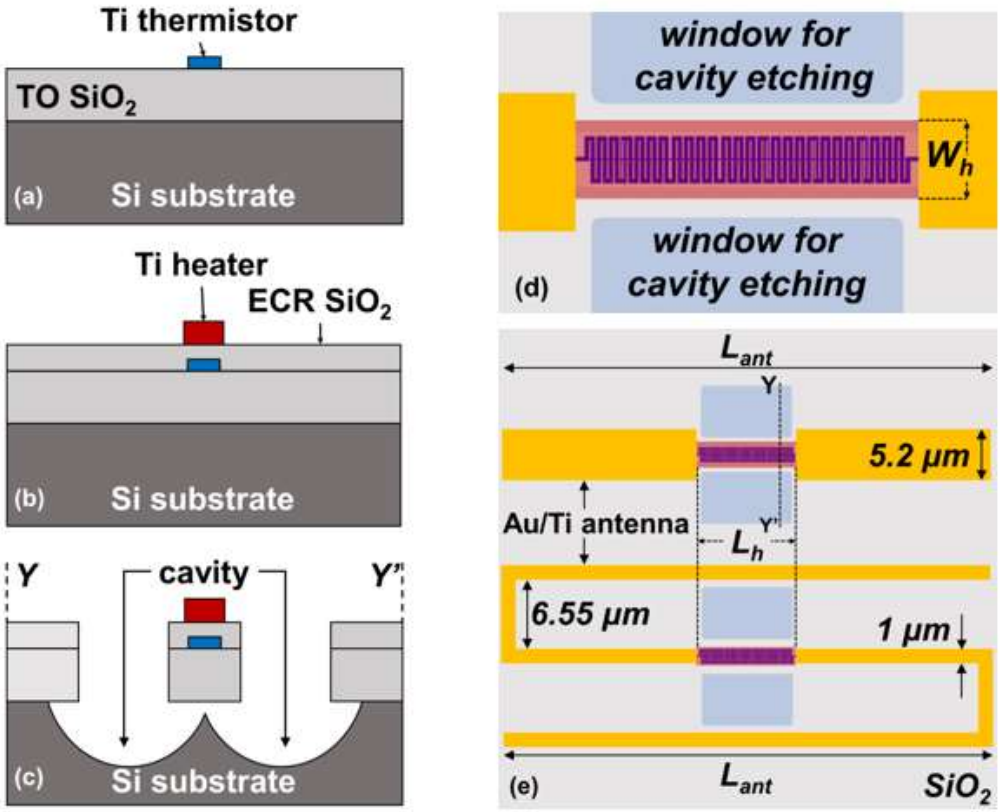


**Fig. 3-3 (a) 50-nm-thick Ti thermistor deposition on top of TO $SiO_2$; (b) Ti heater deposition on top of ECR $SiO_2$ interlayer; (c) Cavity hole fabrication; (d) Heater coupled to the antenna gap on top of meander thermistor; (e) Halfwave dipole antenna (top) and folded dipole antenna (bottom) design structure.**

illustrates the fabricated thermistor on top of TO $SiO_2$. At this point, electrical insulation was then formed by deposition of 100-nm-thick electron cyclotron resonance (ECR) sputtering $SiO_2$ interlayer. Once the interlayer done, heater structure was patterned and deposited, as illustrated

in Fig. 3-3b. Contact hole for thermistor feeding line was patterned and then etched on the interlayer by $CHF_3$ reactive ion etching (RIE). Au antenna and measurement pads were patterned and deposited afterwards. More precisely, a 20 nm Ti thin film was first deposited below the Au thin film to strengthen the adherence of the gold film to the interlayer surface. Finally, deep cavity for thermal isolation was formed by $CHF_3$ RIE and $SF_6$ plasma etching on the $SiO_2$ and Si layers, respectively, as illustrated in Fig. 3-3c. The suspended structure of thermistor and heater was confirmed by the lateral etching during cavity fabrication. All patterning and metal deposition processes were performed by electron beam lithography (JEOL Ltd., JBX-6300SP) and electron beam (Shinko Seiki Co., Ltd., SV-A474) evaporation system, respectively. Fig. 3-3d illustrates the heater design length ($L_{hea}$) with twelve different widths ($W_h$). Two type of antenna in the shape of halfwave and folded dipole with individual antenna length ($L_{ant}$) and width ($W_{ant}$) are illustrated in Fig. 3-3e.

## 3.4 Measurement Method

The material parameters of Ti thermistor and heater were evaluated on a temperature-controlled vacuum prober (Nagase Techno-Engineering Grail 21-205-6-LV-R) outfitted with a precision semiconductor parameter analyzer (Agilent 4156C). A standard IV characterization method were

used to obtain electrical resistance by four probe measurements method on the thermistor and heater current and voltage measurement pads. As the resistance changes with the measurement temperature inside the prober, the TCR (α) which defined as the resistance change factor per degree of temperature change can be calculated by the slope of the linear regression line of resistance against temperature change. Experimentally, TCR was measured by varying the temperature inside the prober from 260 to 300 K in the steps of 10 K.

Electrical responsivity, frequency response, and voltage noise were evaluated at room temperature of 300 K inside the vacuum prober. Since thermistor is commonly designed for all detector devices, bias current ($I_b$) was fixed to 25 μA for all measurements. Responsivity was measured by applying AC electrical power up to 3 μW at a frequency of 10 Hz to the heater and change in thermistor voltage output was observed. A constant current source (Yokogawa GS200) was used to supply the bias current during responsivity measurement and a lock-in amplifier (Signal Recovery 7270) recorded the voltage output from thermistor. Circuit diagram for the electrical responsivity measurement is represented in Fig. 3-4a in constant current (CC) mode. Frequency response of the detector was measured electrically on thermistor by applying amplitude-modulated signal frequency ($f_m$) sweep from 1 to 100 kHz to the heater. The second-

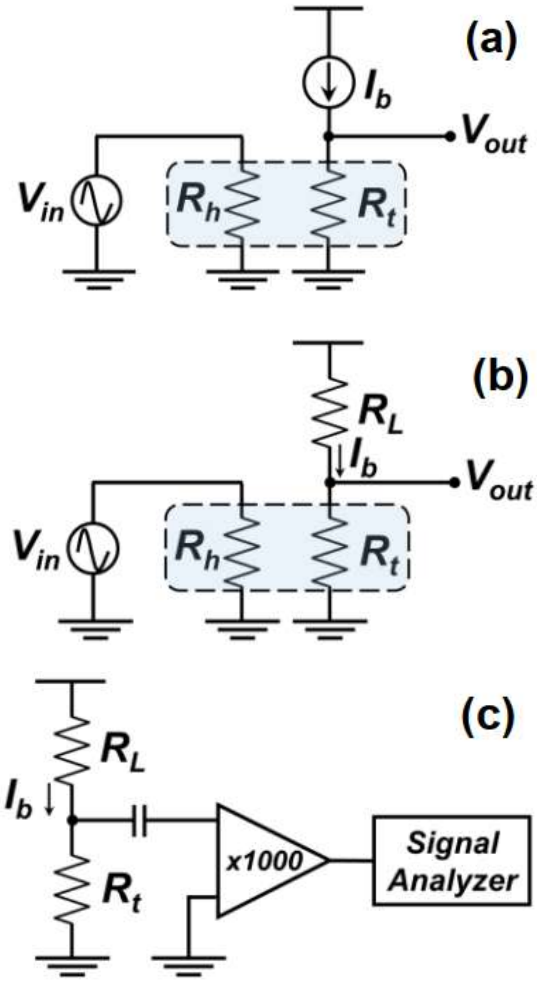


**Fig. 3-4 Equivalent circuits for detector electrical measurements: (a) Circuit for electrical responsivity; (b) Circuit for frequency response; (c) Circuit for noise analysis.**

harmonic thermistor output voltage ($2f_m$) was recorded by a lock-in amplifier because the temperature rise is proportional to the square of the temporal amplitude of the modulated signal. Fig. 3-4b shows the circuit diagram for frequency response measurement with external load resistor

($R_L$) connected in series with thermistor. Voltage noise was recorded on thermistor device over a frequency range of 1 to 100 kHz by an FFT dynamic signal analyzer (Agilent 35670A). Since the thermistor signal amplitude was very low and restricted by the noise produced inside the analyzer, a low-noise and high-gain voltage preamplifier (DL Instruments 1201) was used to improve the sensitivity of the spectrum analyzer. Circuit diagram for the noise measurement is depicted in Fig. 3-4c with the addition of external load resistor ($R_L$) connected in series with thermistor. It is important to note that the external load resistor ($R_L$) of 10 kΩ was connected to thermistor to evaluate frequency response and noise characteristics, and a constant voltage bias source (DL Instruments 1211) was used instead of constant current source.

Responsivity to THz radiation was evaluated by illuminating the backside of the detector chip with THz signal generated from a microwave signal generator (Anritsu MG3692C) operating at 13.2 - 14.9 GHz. An amplifier multiplier chain (VDI AMC 302) has been used to multiply the microwave frequency by 72x and the signal finally excites by a horn antenna (WR1.0 UG-387/UM) at 950 – 1072 GHz range. Detector chip package was installed inside the vacuum dewar and arranged in front of the transmitter antenna at the center of radiation beam spot. The distance between Tx antenna to dewar surface is 70 mm, and the chip package is

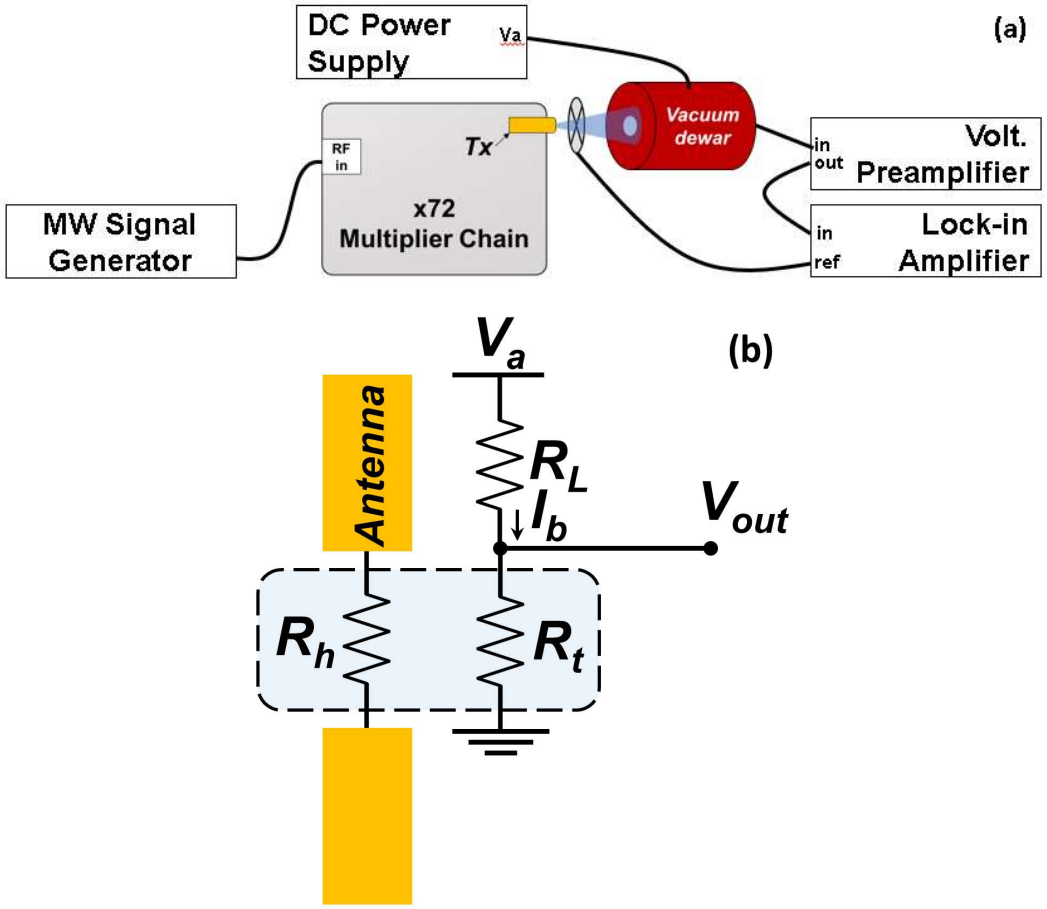


**Fig. 3-5 (a) THz optical responsivity measurement block;**

**(b) Electrical connection inside vacuum dewar.**

mounted 13.5 mm from dewar surface. An optical chopper was placed in between transmitter (Tx) antenna and vacuum dewar window surface to modulate the source radiation and synchronized to the lock-in-amplifier reference input. Typical power radiated from the source is 0.25 mW. However, we employed a calibrated pyroelectric detector (Spectrum Detector SPH-62-THz), with detector area of 20 $mm^2$ to record the radiation intensity at the same place with the detector plane. The incoming

THz radiation from the source had a linear polarization and the E-field component of the detector's antenna was set parallelly to the one from the Tx antenna. A bias current of 25 μA was supplied by the DC power supply constant current source. A voltage preamplifier was used to improve the sensitivity of the lock-in amplifier due to a low output signal intensity generated from thermistor. Fig. 3-5a shows the experimental block for THz measurement. Embedded inside the vacuum dewar is a 100 kΩ load resistor ($R_L$) connected in series to the thermistor ($R_t$) measurement pin as illustrated by the circuit diagram in Fig. 3-5b. No additional optical mirrors nor focusing mechanism used during measurements. It is also important to note the presence of high-density polyethylene (HDPE) window at the vacuum dewar surface that affect the incident THz radiation. Based on the THz-TDS measurement, the HDPE window has 0.88 transmittance value at 1 THz frequency.

## 3.5 Measurement Results

### *3.5.1 Material Parameters*

The maximum input current applied to thermistor and heater were appropriately limited based on the resistance increase up to 3% to avoid overheating and break the devices. A fixed amount of input current was applied to measure thermistor resistance, while the amount of current to

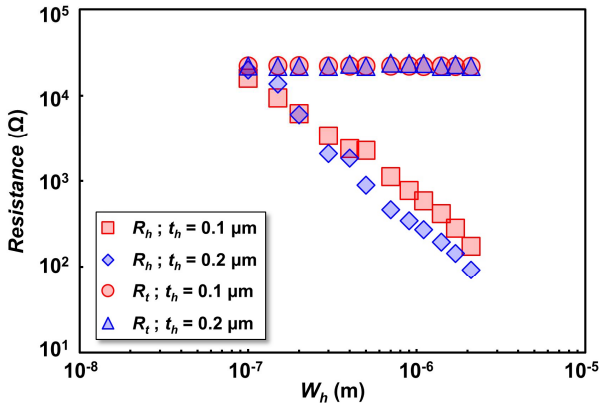


**(a)**

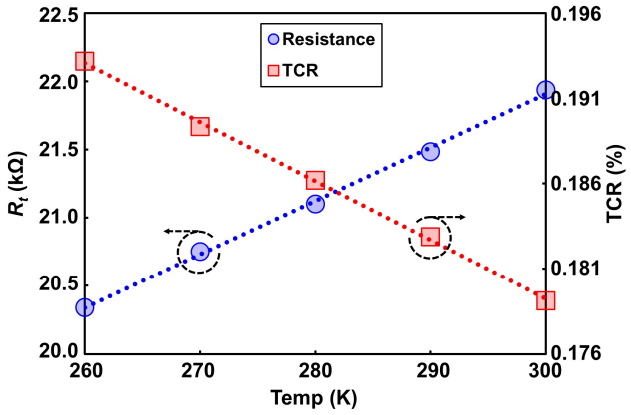


**(b)**

**Fig. 3-6 (a) Thermistor ($R_t$) and heater ($R_h$) resistance dependence on heater width ($W_h$) with different heater thickness ($t_h$); (b) Thermistor resistance and TCR dependence on temperature from 240 K to 300 K.**

heater devices with different widths were set proportionally to the heater widths to obtain constant voltage across them. Resistance at the room temperature ($R_0$) of individual device was taken as the intercept of square input current ($I^2$) against resistance increase. Fig. 3-6a shows the resistance

of the heater ($R_h$) and thermistor ($R_t$) in multiple heater design widths ($W_h$) on 0.1 and 0.2 μm heater thicknesses ($t_h$). $R_h$ are linearly decrease with the increase of $W_h$ as generally expected from the relation between cross-sectional area of the wire and resistance. A slightly lower $R_h$ are shown in the devices with $t_h$ of 0.2 μm due to larger cross-sectional area. However, as observed in narrower $W_h$ devices, some fluctuation of $R_h$ is appeared that could be affected by the interlayer surface roughness above meander thermistor. As for thermistor devices, $R_t$ are slightly fluctuates across different $W_h$ and $t_h$, without any drastic change.

Temperature coefficient of resistance (TCR) of temperature sensor (thermistor) is important material property for a detector as responsivity is proportional to it. TCR represents the resistance relative change per degree of temperature change and can be expressed by the following equation,

$$TCR = \frac{\Delta R}{\Delta T} / R_0, \tag{3-1}$$

where $\Delta R/\Delta T$ is the slope of linear regression line of resistance change. Fig. 3-6b shows the relationship of $R_t$ and TCR against temperature change from 260 K to 300 K with 10 K steps. It is apparent that resistance increases while TCR is slightly reduced with the temperature. Calculated thermistor resistivity and TCR in room temperature were $1.22\times10^{-6}$ Ω.m and 0.179%, respectively, based on the design width of 0.1 μm. There is no drastic TCR

change within different $R_h$, revealed that thermistor electrical parameter is hardly affected by the presence of different heater resistance above it.

### *3.5.2 Electrical Responsivity*

Prior to electrical responsivity measurement, we performed a thermal parameter analysis of the detector. Thermistor, as the detector temperature sensor, is the most important part in the microbolometer structure of this study. Performance measurements were mainly relied on the output given by the thermistor. Hence it is convenient to analyze the thermal resistance of thermistor to predict the detector performance. As the bias current passing through the thermistor, a uniform self-heating reaction in thermistor leads to the resistance and temperature increase, thus output voltage increases due to stimulated heater input power can be obtained. Therefore, thermal property of the thermistor represents the detector performance as it also proportional to the responsivity.

Lateral thermal conductivity ($\kappa$) extraction of a metal wire suspended on a Si substrate has been analyzed based on the average electrical resistance ($\bar{R}$) of the wire under bias current ($I$) expressed by

$$\bar{R} = R_0[(2/mL)tan(mL/2)], \tag{3-2}$$

where $m^2 = I^2 R_0 \alpha/(WdL\kappa)$. Here, $W$, $d$, and $L$ are the width, thickness, and length of the wire, respectively. Equation (3-2) can be further derived

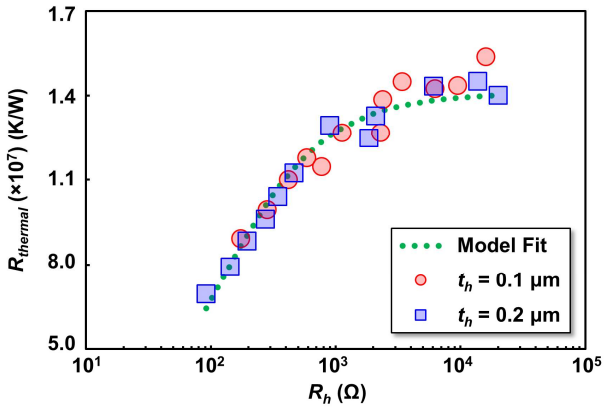


**Fig. 3-7 Measured thermal resistance ($R_{therm}$) of the detectors with different heater resistance.**

by the Taylor expansion of $m$ with respect to $I^2$ into the following expression [15]

$$\bar{R} \backsimeq R_0 \left(1 + \frac{1}{12}\alpha R_0 R_{ther} \quad I^2\right), \tag{3-3}$$

where $R_{therm} = L/(Wd\kappa)$ correspond to the thermal resistance of the wire. Therefore, thermal resistance ($R_{therm}$) calculation of our meander thermistor can be simplified as

$$R_{therm} = \frac{12}{{R_0}^2 \alpha}\left(\frac{dR}{dI^2}\right), \tag{3-4}$$

where ($dR/dI^2$) is the slope of the resistance change for a given square input current [16].

Fig. 3-7 shows the $R_{therm}$ of thermistors calculated by Equation (3-4) with different $R_h$ on 0.1 μm and 0.2 μm heater thicknesses ($t_h$). As shown, $R_{therm}$ of thermistor increases as heater resistance increase. As we use a

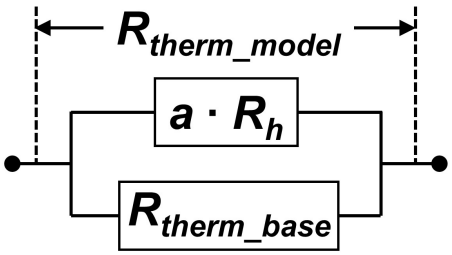


**Fig. 3-8 Thermal resistance model in the microbolometer. $a \cdot R_h$ represents the contribution of thermal resistance from the heater, and $R_{therm\_base}$ represents the contribution of thermal resistance from another detector structure, i.e. thermistor and $SiO_2$.**

common thermistor design with the same electrical parameter, the main contribution to $R_{therm}$ increase is come from the improvement of $dR/dI^2$ in thermistor. It is also revealed that the change in $R_h$ could affect to the temperature increase in thermistor under the same bias current. However, as it also observed, the $R_{therm}$ trend is not linearly to the $R_h$ increase, and a saturated $R_{therm}$ is predictable as the $R_h$ goes very large. At that point, the thermal parameter of the detector is dominated by the other structure such as $SiO_2$ interlayer and substrate, or thermistor. Further analysis of thermal parameter has been made by drawn a fitting line based on a resistor equivalent parallel circuit of thermal resistance contribution from the heater ($R_h$) and another detector structure (i.e. $SiO_2$ and thermistor, hereby symbolized as $R_{therm\_base}$), as illustrated in Fig. 3-8. We assume heater

electrical resistance conversion ratio to its thermal counterpart by a variable of *a*. The model used to predict the calculated thermal resistance ($R_{therm\text{-}model}$) is then given by

$$R_{therm\_model} = \frac{R_{therm\_base} \times (a \times R_h)}{R_{therm\_base} + (a \times R_h)}. \quad (3\text{-}5)$$

The extracted *a* variable is $1.29\times10^5$. This variable can be explained theoretically by the Wiedemann–Franz law that relates the ratio of electrical (σ) to thermal (κ) conductivity parameters of a material (σ/κ = 1/L/T, where L = Lorenz number (2.44 × 10−8 WΩ/K2) and T = temperature) [17]. Given the Lorenz number of $2.44\times10^{-8}$ $W\Omega/K^2$ and experiment temperature of 300K, the electrical to thermal ratio is $1.37\times10^5$ $KW^{-1}\Omega^{-1}$, close to our extracted *a* variable value. As shown in Fig. 3-7, the calculated $R_{therm\_model}$ fits to the measured thermal resistance. This suggests the accuracy of the proposed analytical model for the investigation of thermal contribution in detector for further performance estimation. As for the extracted $R_{therm\_base}$ variable value includes the contribution from the $SiO_2$ and thermistor.

Responsivity of the detector is defined as the ability of thermistor to generate voltage output ($V_{out}$) signals with respect to the applied electrical input power ($P_{in}$). In our detector structure, thermistor is electrically separated but thermally connected to the heater by an $SiO_2$ insulation layer.

Input power that applied to the heater will increase $R_h$ and their average temperature due to Joule heating, hence the heat (power) displaced from the heater stimulates the voltage output increase in thermistor under bias current ($I_b$). Responsivity is proportional to thermistor material parameters such as resistance and TCR as well as the applied bias current. Miniaturization of thermistor by a meander structure had the impact of longer effective length thus increase the resistance with the same lateral length as the stacked heater structure above thermistor. Remind that the gap between the antenna's arm is limited to 11.5 μm. Thinner thermistor has been investigated to have reduced the TCR but increased resistivity. For the present design, we focus on one thermistor design width of 0.1 μm. However, increase of the $R_h$ could also lead to an improvement in responsivity as expected from our previous scaling study. Input power to the heater was given by rising the AC electrical input voltage up to 50 mV at 10 Hz. Thus, the power generated by the heater ($P_{in}$) can be calculated as

$$P_{in} = \frac{{V_{hea}}^2}{R_{hea}}, \tag{3-6}$$

where $V_{hea}$ is the voltage output generated from the heater, and it is obtained by the heater input-output voltage ratio. A constant $I_b$ of 25 μA was applied

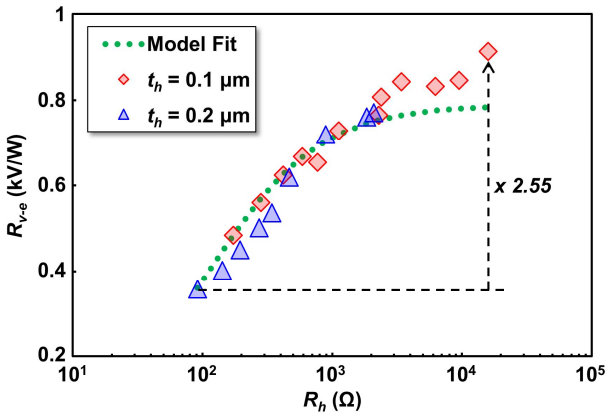


**Fig. 3-9 Detector's electrical responsivity ($R_{v\text{-}e}$) dependence on heater resistance.**

to the thermistor regardless the $R_h$ values. The detector's electrical responsivity ($R_{v\text{-}e}$) is then expressed by

$$R_{v-e} = \frac{V_{out}}{P_{in}}. \tag{3-7}$$

As $P_{in}$ increase, the thermistor $V_{out}$ will also increase. Therefore, slope of $V_{out}$ against $P_{in}$ gives the $R_{v\text{-}e}$. Fig. 3-9 shows the $R_{v\text{-}e}$ variation with different $R_h$. Maximum $R_{v\text{-}e}$ increase of 2.55 times is observed as the $R_h$ increase up to 16 kΩ. The $R_{v\text{-}e}$ enhancement, however, is nearly proportional to the extracted detector's thermal resistance in Fig. 3-7. It revealed that thermal resistance measured on thermistor is proportional to the detector's responsivity. The maximum responsivity is 913 V/W from the device with $R_h$ of 16 kΩ. The calculated responsivity was also given by the model described previously in Equation (3-5), with an additional proportionality constant of $b$ is added in series to represent the conversion factor of

temperature rise to the output voltage [13]. The analytic model for responsivity ($R_{v\_model}$) is then given by

$$R_{v\_model} = R_{therm\_model} \times b. \quad (3\text{-}8)$$

As can be seen in Fig. 3-9, the calculated responsivity by the proposed model fits to the measurement results, suggesting the effectiveness of the model in Equation (3-8) to predict the responsivity trend. The extracted $b$ variable is $5.6\times10^{-5}$. It is close to the theoretical extended responsivity analysis calculation from the product of applied bias current ($I_b$), extracted TCR ($\alpha$), and thermistor resistance ($R_t$), and some additional factor that close to the 1/12 based on Equation (3-4). This additional factor came from the temperature rise in meander thermistor is mainly located at the center part and not in the entire thermistor. One concern about the $R_{v\text{-}e}$ results in Fig. 3-9 is that three heater devices with the heater width of 0.1, 0.15, and 0.2 μm and thickness of 0.2 μm were defected and unable to be measured. However, their performance can be predicted based on the close proportionality of Fig. 3-7 and 3-9.

Figure 3-10a shows the measured thermistor output voltage ($V_{out}$) response to the change in input AC frequency ($f$) applied to the heater. Since the load resistor ($R_L$) was connected in series with thermistor ($R_t$) according to Fig. 3-4b, the effect of $R_L$ has been eliminated by estimating the output voltage in CC. The cut off frequency ($f_c$) was used as the fitting

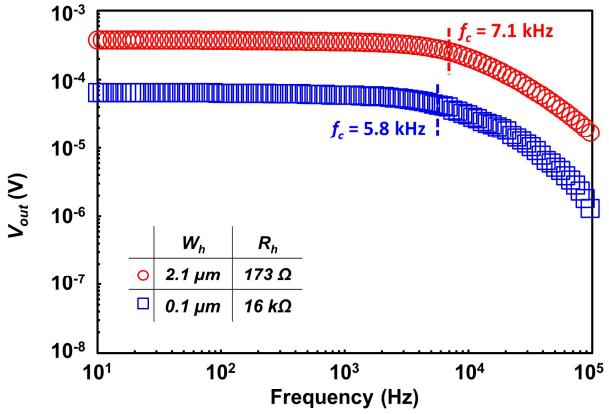


**(a)**

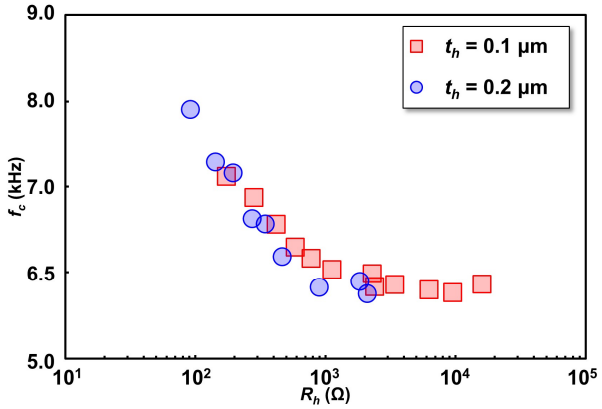


**(b)**

**Fig. 3-10 (a) Thermistor output voltage to the change of temperature fluctuation frequency, estimated in CC mode; (b) Detector's cut off frequency (fc) dependence to heater resistance.**

parameter to minimize the error between the measured ($V_o$) and calculated output voltage $|V_{out}(f)|$ by the following fitting equation,

$$|V_{out}(f)| = \frac{|V_o|}{\sqrt{1+\left(\frac{f}{f_c}\right)^2}}. \quad (3\text{-}9)$$

The $f_c$ that gives minimum error extracted as the cut off frequency. It is notable that higher $R_h$ with higher responsivity has smaller $f_c$ thus earlier response roll-off is observed. The cut off frequency ($f_c$) dependence to $R_h$ is shown in Figure 3-10b. As shown, $f_c$ decreases as $R_h$ increases, which is opposite to that of responsivity. This can be explained by the lower thermal diffusivity characteristic of the $SiO_2$ compared to Ti from the heater [18]–[20]. As the Ti heater width narrower ($R_h$ increase), the volumetric ratio between Ti and $SiO_2$ becomes smaller and the heat generated in the heater is diffused slower. It is also important to note that the extracted $f_c$ is based on the temperature fluctuation frequency which is double the AC frequency applied to the heater. Additionally, the measured $f_c$ can be further adapted to extract the detector's thermal response time ($\tau$) by the relation of $1/2\pi f_c$. Indicating that the faster response can be expected for the detector with higher $f_c$.

### 3.5.3 Noise Characteristics

Noise equivalent power (NEP) is defined as the input power that gives a signal-to-noise ratio of one for the output noise of 1 Hz. The NEP is the main figure-of-merit of a detector's sensitivity and can be expressed by

$$NEP = \frac{V_n}{R_v}, \tag{3-10}$$

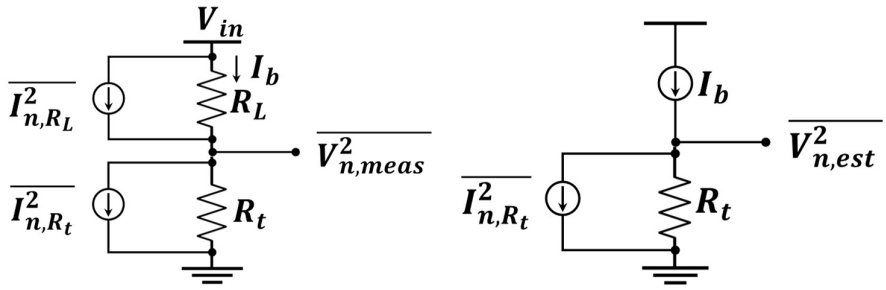


**(a)** **(b)**

**Fig. 3-11 (a) Equivalent circuit diagram for noise measurement in $R_L$ mode; (b) Equivalent circuit diagram for noise estimation in CC mode.**

where $V_n$ is the voltage noise recorded at thermistor device for a given bias current. A 10 kΩ external $R_L$ was connected in series with thermistor, as previously shown in Fig. 3-4c. The recorded voltage noise has been converted to the constant current (CC) voltage noise mode thus eliminate the effect of the $R_L$. Fig. 3-11 (a) and 3-11 (b) show equivalent circuit diagram for noise measurement in $R_L$ mode and estimation of noise in CC mode, respectively. According to Fig 3-11 (a), the measured noise voltage with load resistor connected can be expressed as

$$\overline{V^2_{n,meas}} = \left(\overline{I^2_{n,R_t}} + \overline{I^2_{n,R_L}}\right) \times (R_L||R_t)^2 \tag{3-11}$$

where the current passing through the load resistor ($R_L$) is given by

$$\overline{I_{n,R_L}} = \sqrt{4k_B T/R_L} \tag{3-12}$$

Here we assume that the load resistor ($R_L$) generates ideal thermal noise. Finally, the estimated noise in CC mode based on Fig. 3-11 (b) is

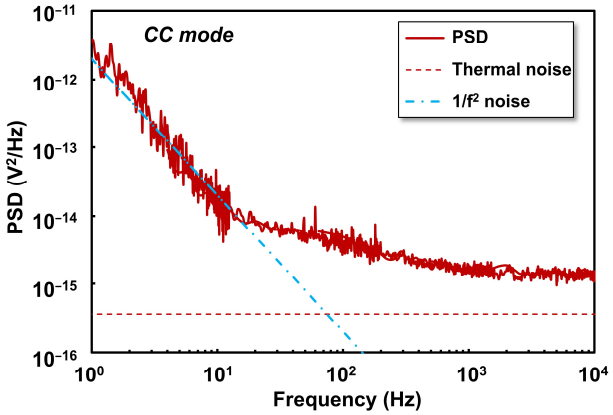


**(a)**

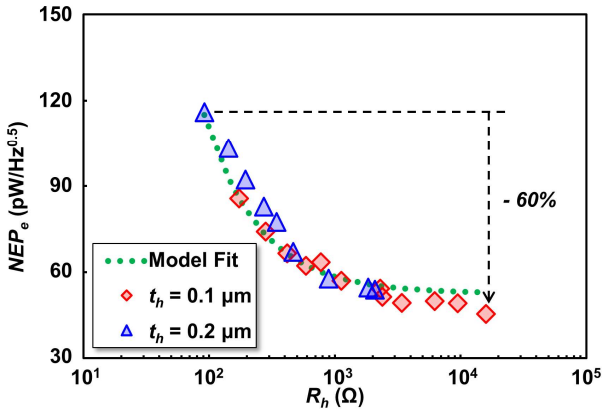


**(b)**

**Fig. 3-12 Noise evaluation of the detector: (a) Power spectrum density (PSD) estimated in CC mode; (b) Electrical noise equivalent power ($NEP_e$) evaluated at 1 kHz.**

$$\overline{V_{n,est}^2} = \overline{I_{n,R_t}^2} \times R_t^2 \tag{3-13}$$

Figure 3-12 (a) shows the estimated power spectrum density (PSD) in CC mode of the detector under 25 μA thermistor bias current. The theoretical

noise ($V_{n\_therm}$) floor was assumed to be thermal noise generated from $R_t$ and given by

$$V_{n\_therm} = \sqrt{4k_B T R_t}, \tag{3-14}$$

where $k_B$ is the Boltzmann constant and $T$ is the room temperature during measurement. At low frequencies below 10 Hz, the noise power is increase almost proportional to the $1/f^2$ noise that might be caused by the characteristics of a narrow metal wires. At high frequencies, the noise spectrum becomes flat reflecting the "white" characteristics of thermal and shot noises close to the theoretical thermal noise. Fluctuations in the noise spectra are came from the environmental noise in the measurement setup. Fig. 3-12 (b) shows the NEP of the detector against $R_h$ change. Assuming the flat response of the detector at the frequency below the $f_c$, the NEP was evaluated at 1 kHz with the corresponding voltage noise ($V_n$) of $4.15\times10^{-8}$ $V/Hz^{0.5}$. The lowest NEP is 45.5 $pW/Hz^{0.5}$ from the device with $R_h$ of 16 kΩ. The calculated maximum NEP reduction is nearly the same as the responsivity improvement due to the common voltage noise in thermistor. The fitting line for NEP results trend was added based on the voltage noise divided by the same model applied for electrical responsivity fitting in Equation (3-8). As also observed in Fig. 3-12 (b), the calculated NEP

model is fit to the measured NEP as it is inversely proportional to the responsivity.

### 3.5.4 THz Characterization

Twelve different heater widths were characterized for electrical measurements. However, we used four different heater widths in each heater thicknesses for THz characterization using two antenna type. The chosen heater widths correspond to the heater resistance near to the antenna's resonant resistance. Prior to the THz measurements, a calibration of the pyroelectric detector (PED) responsivity was performed. The PED is used to record the incident power density at the detector plane. This method offers the flexibility to calculate the input power without the need-to-know exact transmitter system characteristics, as long as the light receiving area is clearly defined or sufficiently larger than the incoming light spot. After that, the 1 THz radiation intensity is measured at the detector place by using PED. The recorded voltage signal by PED together with the PED responsivity will result in the radiation intensity on the detector plane. Finally, the proposed THz microbolometer can be measured. The steps for THz characterization are briefly summarized in Fig. 3-13.

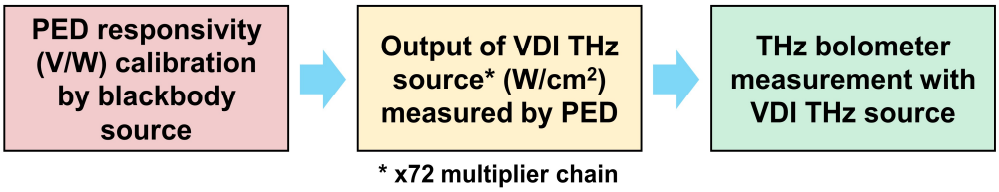


**Fig. 3-13 THz characterization steps taken for measuring the detector.**

***PED Calibration***

PED generally shows rather flat response over a broad range of wavelengths. The sensitivity is relatively high among room-temperature detectors. It is reasonable to calibrate a PED for the optical power measurement in the THz regime before use it for power density measurement. Fig 3-14 shows the measurement setup for PED calibration by using blackbody radiation source. The PED type is SPH-62-THz made of LiTaO3 pyroelectric crystal on a ceramic substrate, from Spectrum Detector Inc. The light source is a standard blackbody furnace SR-2-33-SP from CI System. The voltage output of the detector was measured by a lock-in mechanism using Signal Recovery 7270 lock-in amplifier (LIA). The filters used are black polyethylene, quartz and a 1 THz band pass filter (MMBPF40-1000). These THz filters were used to verify the responsivity in THz region thus neglecting the contribution of the other frequency components in the blackbody infrared spectrum. The position of the PED is aligned so that the detection element is at the center of the focal point of

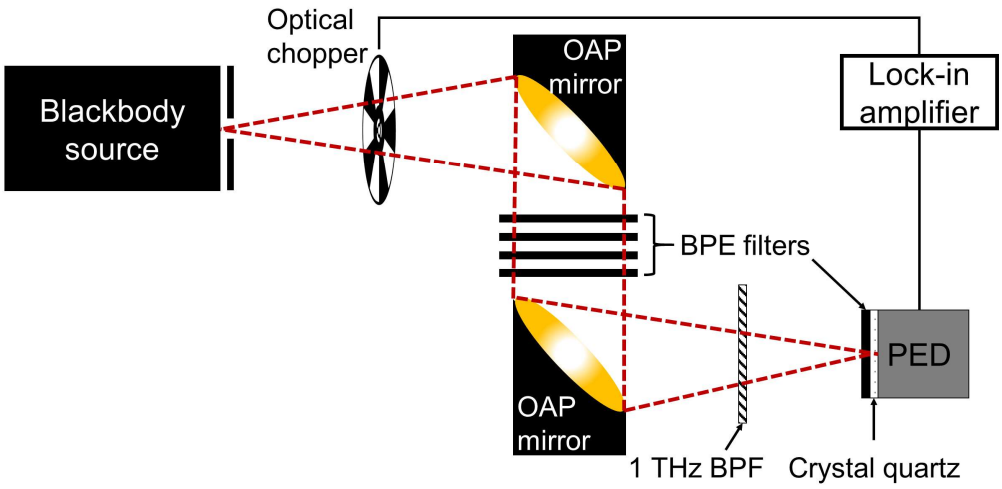


**Fig. 3-14 Pyroelectric detector (PED) responsivity calibration setup by using blackbody radiation source.**

the focusing parabolic mirror. Total propagation distance from the blackbody aperture point to the PED aperture surface is 29.5 cm. The measurement was carried out at room temperature of 297 K while the blackbody radiation temperature was varied from 600 to 1000 K with 100 K interval. The modulation frequency was varied from 3 to 300 Hz.

The incident power from the blackbody source falling to the detector can be calculated as the product of blackbody irradiance, transmittance of the optical components and propagation medium, and the solid angle of the off-axis parabolic mirrors. The wavelength dependent variable such as blackbody radiance spectrum and optical transmittance are numerically integrated over the infrared wavelength from 1 to 500 μm (300 to 0.6 THz) as it coincides with the operational wavelength of the PED. The

temperature dependent total incident power ($P_{in}(T)$) of the blackbody source can be formulated as

$$P_{in}(T) = \Omega \cdot t_{air} \cdot A_D \cdot \int_{\lambda_1}^{\lambda_{500}} E_T(\lambda) \cdot t_{filte} \quad (\lambda) d\lambda \tag{3-15}$$

where $\Omega$, $t_{air}$, $A_D$, and $t_{filters}$ are the solid angle of the OAP mirror [sr], transmittance of the propagation medium (air), detector size area [$m^2$], and transmittance of the filters. The wavelength and temperature dependent blackbody radiance ($E(\lambda, T)$) can be calculated based on the Planck's blackbody radiation law as

$$E(\lambda, T) = \frac{2hc^2}{\lambda^5} \frac{1}{\exp(^{hc}/_{\lambda k_B T}) - 1} \text{ [W/cm}^2\text{/sr/μm]} \tag{3-16}$$

where $h$ is Planck's constant [J/s], $c$ is the speed of light [m/s], and $k_B$ is the Boltzmann's constant [J/K]. As the measurement was performed in the room temperature, the intensity was obtained by subtracting each blackbody radiance in the temperature under test (600 to 1000 K) with the background radiation intensity at 297 K temperature.

Fig. 3-15 presents the transmittance of the BPE, crystal quartz plate, and 1 THz BPF. The transmittance of the BPE was obtained by FTIR and THz-TDS, the transmittance of the crystal quartz plate was provided by measurement data of Infrared Laboratories and THz-TDS, and the

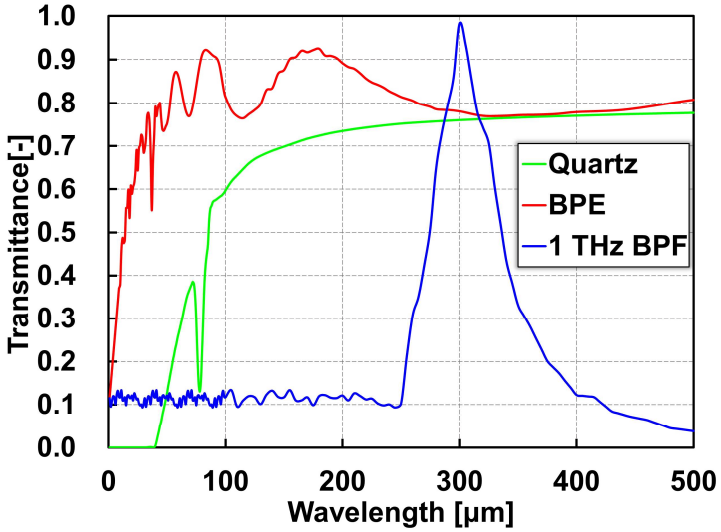


**Fig. 3-15 Filter transmittance of BPE, quartz, and BPF used during PED responsivity calibration.**

transmittance of BPF was provided by the manufacturer and validated by THz-TDS measurement.

The transmittance along propagation medium (air) determined based on the Beer-Lambert law of optical attenuation to accurately calculate the absorption by the water vapor. The atmospheric transmittance of the air is described as

$$t_{air} = \exp(-N \cdot \alpha_{clm}) \tag{3-17}$$

where $N$ is the column density of water [$m^{-2}$] and $\alpha_{clm}$ [$m^2$] is the absorption coefficient. The column density calculation can be derived from the ideal gas law as

$$N \approx 7.2426 \times 10^{16} \frac{p_{H_2O}(T)}{T} L[/m^2] \tag{3-18}$$

where $L$ is the total propagation distance of the optical measurement setup and $p_{H_2O}$ is the saturated water vapor pressure [Pa] in temperature of $T$.

The energy falls on the detector surface is also affected by the area of the detector element ($A_D$) and the solid angle ($\Omega$) of the parabolic mirror because the beam spot of the blackbody radiation is sufficiently larger than the detector area. The solid angle can be calculated by

$$\Omega = \frac{\pi}{4F+1} \text{ [sr]} \tag{3-19}$$

where $F$ is the F-number of the focusing parabolic mirror, obtained from the radius and focal length of the mirror. The room temperature and humidity were 24 C and 57%, respectively, during experiment. The calculated column density and saturated water vapor were $1.2\times10^{18}$ $cm^{-2}$ and 2984 Pa, thus the atmospheric transmittance was calculated to be 0.6934. The calculated solid angle ($\Omega$) of the parabolic mirror was 0.0655 sr and aperture area of the PED ($A_D$) is 2x2 $mm^2$, as provided by the manufacturer.

The voltage responsivity of PED ($R_{v\_PED}$) was calculated based on the ratio of the voltage output signal of the PED to the incident power from blackbody source modulated by optical chopper. Fig. 3-16 shows the calibrated responsivity of the PED as a function of temperature and chopping frequency. The responsivity decreases with the modulation

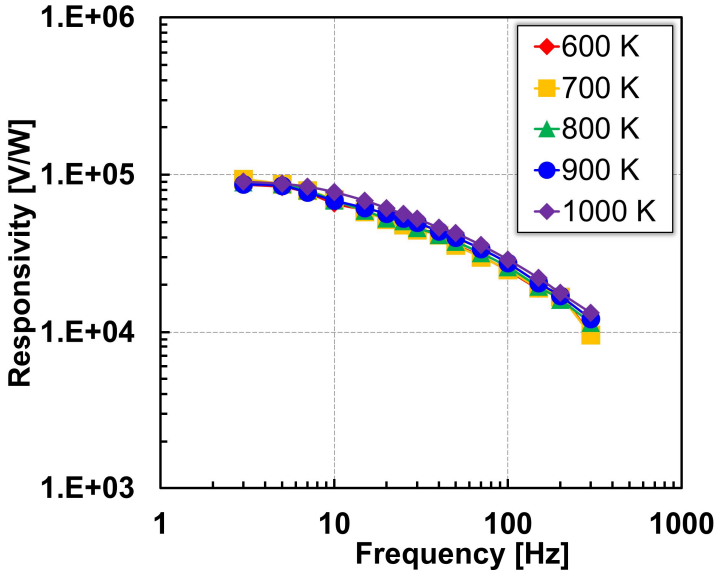


**Fig. 3-16 Responsivity of PED calibrated at different temperature and modulation frequency.**

frequency and it is barely affected by the blackbody temperature. The absolute responsivity obtained after calibration is 89 kV/W [21].

***THz Optical Responsivity Measurements***

Figure 3-17 shows the measurement of radiation intensity of the 1 THz source by PED. The PED is placed on the 3-axis stage and aligned in the position where the THz microbolometer will be installed. Experimentally, the voltage signal output from the PED was recorded at the frequency range of 950–1073 GHz where the THz radiation source is applied. Assuming the flat responsivity of the PED across the frequency range, we can obtain the incident power in the same frequency range. The

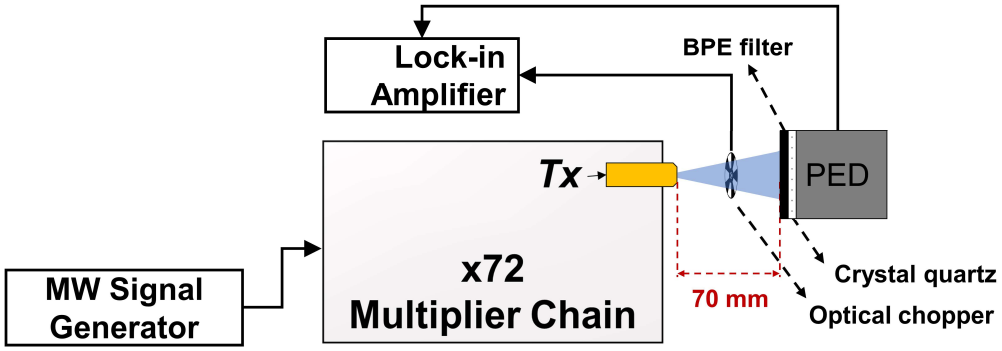


**Fig. 3-17 Radiation intensity measurement of 1 THz source by using PED.**

distance between tip of Tx horn antenna to the PED box surface is 70 mm. However, the actual pyroelectric sensor element inside the box is located 14.9 mm from the surface.

Figure 3-18 shows the setup of the optical experimental using THz source and vacuum dewar where the THz microbolometer is installed. The distance between THz transmitter antenna to dewar surface is 70 mm. The actual bolometer surface inside the dewar is located 13.5 mm from the dewar surface. Note that a high-density polyethylene (HDPE) window is present in the vacuum dewar surface with 0.88 transmittance at 1 THz frequency. As in the previous electrical characterization, THz optical responsivity is defined as the thermistor voltage output with respect to the input power given by the heater. Instead of direct power supplied to the heater, the THz input power generated from the heater is taken from the capability of the antenna to capture incoming THz radiation from the

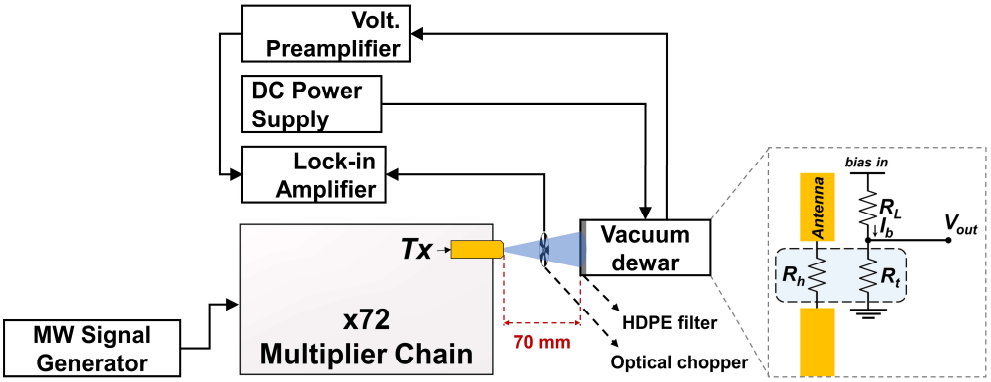


**Fig. 3-18 Optical responsivity measurement setup by using 1 THz radiation source. Bolometer chip is mounted inside vacuum dewar.**

source to be further transferred into the heater. A good impedance matching between heater and antenna is critical, as one can expect a good power transfer between the two [22]. The output power stated by the THz source equipment datasheet might come to an overestimated value, since not all the incident power falling on detector's plane is captured by the antenna. Only a portion of power within the effective antenna area will be absorbed then transferred to the heater load on the antenna gap under good impedance matching. Assuming the THz wave is radiated in uniform power density towards detector's plane, the amount of absorbed power by the antenna can be known if the effective area of the antenna is determined. Experimentally, we recorded the incident power density ($W_{in}$) by using a calibrated pyroelectric detector (PED) at the same position where vacuum

dewar was installed. The light receiving area ($A_e$) used to calculate input power is assumed as diffraction-limited area based on the square of the effective wavelength on the detector's surface ($\lambda_s^2$) [23]. The maximum calibrated $W_{in}$ within THz source frequency range in detector position was 25 μW/cm$^2$. The THz optical input power ($P_{in\text{-}o}$) is then given by the following equation

$$P_{in-o} = W_{in} \times A_e. \tag{3-20}$$

The incoming THz radiation from the source had a frequency of 1 THz. Given the relative permittivity of Si substrate of 11.7, the effective wavelength ($\lambda_s$) on the detector's surface is 119 μm. Finally, THz optical responsivity ($R_{v\text{-}o}$) can be calculated based on the thermistor voltage output divided by the $P_{in\text{-}o}$. The PSD profile for optical NEP is taken from the estimated PSD with 100 kΩ load resistor ($R_L$) based on the PSD result in electrical measurement ($R_L$ = 10 kΩ). Equation (3-13) is used to estimate the noise voltage for different load resistor. The obtained voltage noise at 1 kHz is $3.48\times10^{-08}$ V/Hz$^{0.5}$. Fig. 3-19 (a) and 3-19 (b) show the $R_{v\text{-}o}$ and NEP trend with the change in $R_h$ for the detector coupled to the halfwave dipole antenna. A declining trend is shown for the $R_{v\text{-}o}$ results, revealed the ability of the halfwave dipole antenna to transfer the incoming THz power optimally to low resistance heaters. The maximum $R_{v\text{-}o}$ and $NEP_o$ for halfwave dipole antenna-coupled detector is 530 V/W and 42 pW/Hz$^{0.5}$,

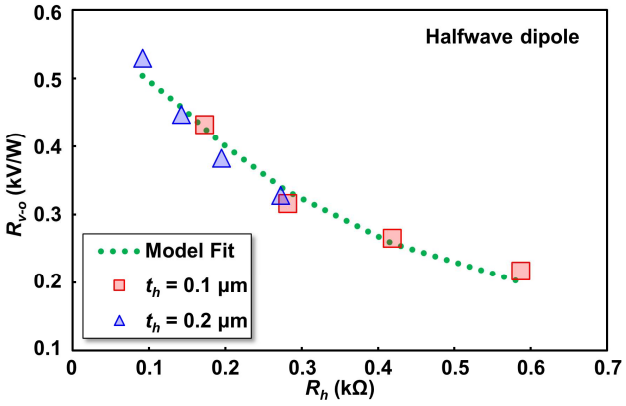


**(a)**

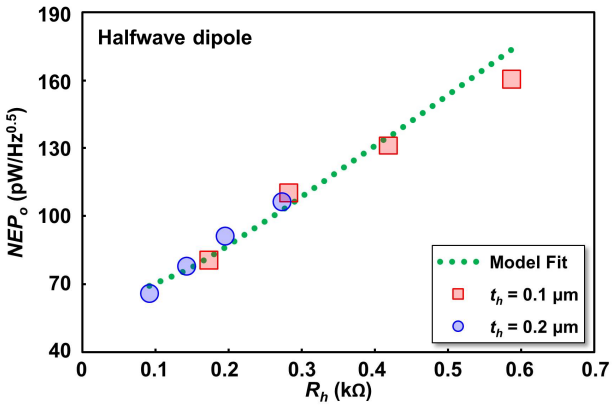


**(b)**

**Fig. 3-19 (a) THz optical responsivity ($R_{v\text{-}o}$) and (b) NEP dependence on heater resistance for antenna-coupled halfwave dipole antenna.**

respectively, from the device with $R_h$ of 91 Ω. Fig. 3-20 (a) and 3-20 (b) show the $R_{v\text{-}o}$ and $NEP_o$ trend with the change in $R_h$ for the detector coupled to folded dipole antenna (FDA). A maximum $R_{v\text{-}o}$ and $NEP_o$ were observed at the heater resistance of 586 Ω, close to the simulated resonant resistance of FDA (675 Ω). The $R_{v\text{-}o}$ and $NEP_o$ performance worsened as the $R_h$ far

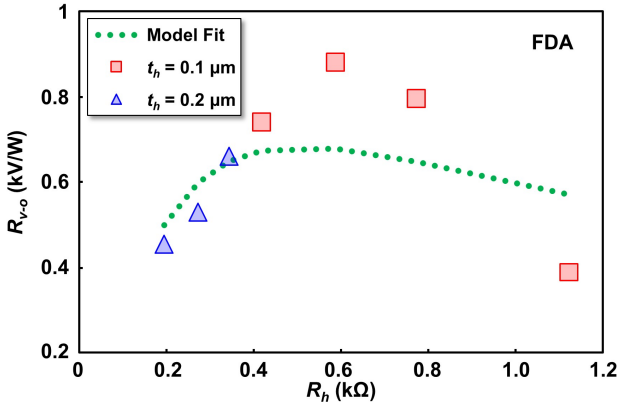


**(a)**

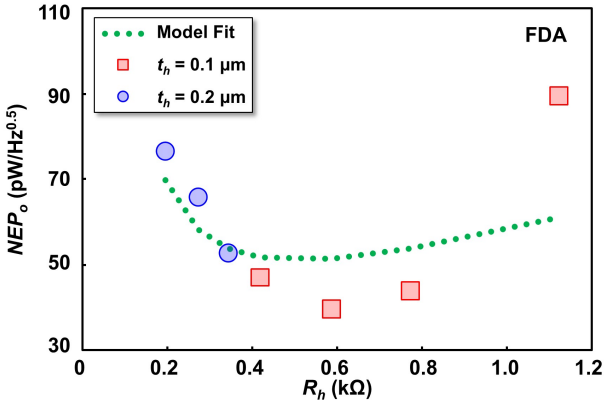


**(b)**

**Fig. 3-20 (a) THz optical responsivity ($R_{v\text{-}o}$) and (b) NEP dependence on heater resistance for antenna-coupled halfwave dipole antenna.**

away from the resonant point. These results indicate that the designed antennas could effectively transfer the incident THz energy to the heater according to their resonant characteristics and matching heater resistance. The maximum $R_{v\text{-}o}$ and $NEP_o$ for folded dipole antenna-coupled detector is 882 V/W and 39 pW/Hz$^{0.5}$, respectively.

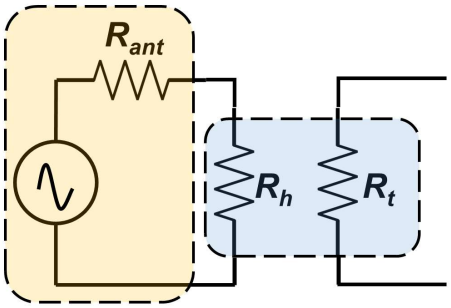


**Fig. 3-21 Illustration of circuit diagram for heater input power modelling in THz characterization.**

Further analysis was taken by the model fit line based on the Equation (3-21). Additional circuit diagram illustrated in Fig. 3-21 is considered due to the fact that input power to the heater was mainly contributed by the antenna, and impedance matching between the antenna and heater significantly affect the THz input power. The input power (power consumption in the heater) can be estimated based on the input voltage ($V_{in}$) generated at the antenna gap and both antenna ($R_{ant}$) and heater ($R_h$) resistances. Given the responsivity model in Equation (3-8) and circuit diagrams in Fig. 3-17 for THz input power, the THz optical responsivity fitting model ($R_{v\text{-}o\_model}$) can be summarized by the following equation

$$R_{v-o\_model} = R_{v\_model} \times \frac{4R_{ant}R_h}{(R_{ant}+R_h)^2} \times c. \quad (3\text{-}21)$$

The extracted $R_{v\text{-}o\_model}$ was obtained by changing the $R_{ant}$ and $c$ variable to minimize the discrepancies between measured optical responsivity ($R_{v\text{-}o}$)

and calculated optical responsivity ($R_{v\text{-}o\_model}$). Note that extracted $b$ variable from Equation (3-8) together with $R_{therm\_base}$ and $a$ variables from Equation (3-5) are included in Equation (3-21) because the thermistor design is identical and so the thermal contribution parameters also the same. The extracted value of $R_{ant}$ for the halfwave dipole antenna device is 20, which is close to the simulated resonant resistance result in Fig. 3-2. While the extracted value of $R_{ant}$ for FDA is 358 which is far from the simulated resonant resistance of FDA. As for the optical NEP results fitting trend were taken by dividing the estimated voltage noise in 100 kΩ RL mode with the calculated responsivity in Equation (3-21). From the graph in Fig. 3-19 (a) and 3-19 (b), the proposed model fit to the THz optical responsivity and NEP for halfwave dipole antenna. Inevitably, there were some higher discrepancies found for fitting the results of FDA in Fig. 3-20 (a) and 3-20 (b) due to the limitation of our proposed model for the high-impedance antenna and the extracted $R_{ant}$ for FDA that shifted from the resonant resistance based on the electromagnetic simulation.

The maximum THz responsivity was found in the heater resistance of 586 Ω, while the electrical measurement results reveal a better improvement with the higher heater resistance. A higher impedance antenna thus can be expected to further improve the THz responsivity. However, our main intention in this study was to assess the importance of

**Table 3.2 Comparison with other room-temperature THz detectors**

| Sensor Material | $R_v$ (V/W) | NEP (pW/$\sqrt{Hz}$) | Freq (THz) | Pixel | Antenna | Resp. time | Ref. |
|---|---|---|---|---|---|---|---|
| Ti | 90 | 460 | 1 | Single | Dipole | 22.7 µs | [6] |
| VOx | 331 | 123 | 2.5 | Single | Patch | 6.7 ms | [24] |
| $Nb_5N_6$ | 113 | 44 | 0.64 | 250×250 | Double-slot | - | [25] |
| $Si_3N_4$ | - | 100 | 0.14 | Single | MEMS resonator | - | [26] |
| YBCO | 45 | 50 | 0.4 | Single | Log-spiral | - | [27] |
| Graphene | 2 mA/W | - | 2 | 44×37 | Dipole | - | [28] |
| PTAT sensor | 46.5 | 1260 | 2.6 | Single | Loop antenna | 330 ms | [29] |
| Ti | 881 | 39 | 1 | Single | Folded-dipole | 25.3 µs | This work |

heater resistance increase to the detector's responsivity, and effectiveness of the folded dipole antenna with the high resistance heater compared to the classic halfwave dipole antenna. The results highlighted in the present study, nevertheless, also make several noteworthy contributions for the further design consideration towards higher detector's performance.

Table 3.2 shows the performance comparison of the proposed detector with the other THz bolometric detectors. The proposed detector has the advantage of high responsivity compared to the other metal-based THz bolometers for a single pixel element. However, the noise performance is still high compared to the target other novel metal bolometers. Our target to develop THz detector with one order of NEP is

challenging as the noise and responsivity are inversely proportional to each other. One possible reason of the high noise characteristics is the high environmental noise during measurement. Further measurement adjustment needs to be considered to suppress the environmental noise and improve the NEP.

## 3.6 Conclusion

Multiple detector devices have been fabricated and studied. The electrical measurement results showed a simultaneous performance improvement in responsivity and NEP up to 2.5 times by combination of 0.1 μm wide straight heater with a 0.1 μm wide meander thermistor. Performance comparison between low and high resistance heater to THz radiation has been analyzed by using a FDA and a halfwave dipole antenna, revealed that responsivity could be optimally improved with a matching impedance of antenna and heater. Moreover, our simple circuit model reveals that enhancement in responsivity was primarily obtained owing to the improvement in the thermal resistance. However, as the heater resistance goes very large, responsivity was saturated suggesting the thermal conduction of the detector is dominated by the other device structure. Prospective future improvements are suggested by removing the $SiO_2$ interlayer and integrate thermistor and heater into a single structure.

## References


[1] R. A. Wood, "Chapter 3 Monolithic Silicon Microbolometer Arrays," in *Semiconductors and Semimetals*, vol. 47, 1997, pp. 43–121d. doi: 10.1016/S0080-8784(08)62689-7.

[2] R. K. Bhan, R. S. Saxena, C. R. Jalwania, and S. K. Lomash, "Uncooled infrared microbolometer arrays and their characterisation techniques," *Defence Science Journal*, vol. 59, no. 6, pp. 580–589, 2009. doi: 10.14429/dsj.59.1562.

[3] P. W. Kruse, *Uncooled Thermal Imaging Arrays, Systems, and Applications*. Bellingham, USA: SPIE Press, 2001.

[4] D. P. Neikirk, W. W. Lam, and D. B. Rutledge, "Far-infrared microbolometer detectors," *International Journal of Infrared and Millimeter Waves*, vol. 5, no. 3, pp. 245–278, Mar. 1984, doi: 10.1007/BF01009656.

[5] M. V. S. Ramakrishna, G. Karunasiri, P. Neuzil, U. Sridhar, and W. J. Zeng, "Highly sensitive infrared temperature sensor using self-heating compensated microbolometers," *Sensors and Actuators A: Physical*, vol. 79, no. 2, pp. 122–127, Feb. 2000, doi: 10.1016/S0924-4247(99)00280-0.

[6] N. Hiromoto, A. Tiwari, M. Aoki, H. Satoh, M. Takeda, and H. Inokawa, "Room-temperature THz antenna-coupled microbolometer with a Joule-heating resistor at the center of a half-wave antenna," in *2014 39th International Conference on Infrared, Millimeter, and Terahertz waves (IRMMW-THz)*, Sep. 2014, pp. 1–2. doi: 10.1109/IRMMW-THz.2014.6956173.

[7] M. Aoki, M. Takeda, and N. Hiromoto, "Electromagnetic Simulation for THz Antenna-Coupled Microbolometers Operated at Room Temperature," *MAKARA Journal of Technology Series*, vol. 17, no. 1, Sep. 2013, doi: 10.7454/mst.v17i1.1919.

[8] Y. L. Cheng, B. J. Wei, F. H. Shih, and Y. L. Wang, "Stability and Reliability of Ti/TiN as a Thin Film Resistor," *ECS Journal of Solid State Science and Technology*, vol. 2, no. 1, pp. Q12–Q15, Nov. 2013, doi: 10.1149/2.022301jss.

[9] A. Tanaka *et al.*, “Infrared focal plane array incorporating silicon IC process compatible bolometer,” *IEEE Transactions on Electron Devices*, vol. 43, no. 11, pp. 1844–1850, 1996, doi: 10.1109/16.543017.

[10] J. Trontelj, G. Valušis, R. Venckevičius, I. Kašalynas, A. Sešek, and A. Švigelj, “A high performance room temperature THz sensor,” in *Proc. SPIE 9199, Terahertz Emitters, Receivers, and Applications V*, Sep. 2014, p. 91990K. doi: 10.1117/12.2060692.

[11] A. Tiwari, H. Satoh, M. Aoki, M. Takeda, N. Hiromoto, and H. Inokawa, “THz Antenna-Coupled Microbolometer with 0.1-µm-wide Titanium Thermistor,” *International Journal of ChemTech Research*, vol. 7, no. 2, pp. 1019–1026, Feb. 2014, [Online]. Available: http://hdl.handle.net/10297/9268

[12] A. Banerjee *et al.*, “Width dependence of platinum and titanium thermistor characteristics for application in room-temperature antenna-coupled terahertz microbolometer,” *Japanese Journal of Applied Physics*, vol. 56, no. 4S, Apr. 2017, doi: 10.7567/JJAP.56.04CC07.

[13] A. Banerjee, H. Satoh, Y. Sharma, N. Hiromoto, and H. Inokawa, “Characterization of platinum and titanium thermistors for terahertz antenna-coupled bolometer applications,” *Sensors and Actuators A: Physical*, vol. 273, pp. 49–57, Apr. 2018, doi: 10.1016/j.sna.2018.02.014.

[14] A. P. Aji, H. Satoh, C. Apriono, E. T. Rahardjo, N. Hiromoto, and H. Inokawa, “Performance Improvement of THz Microbolometer by Folded-Dipole Antenna,” in *68th JSAP Spring Meeting*, 2021, pp. 18p-Z09-2.

[15] W. Liu and M. Asheghi, “Thermal conduction in ultrathin pure and doped single-crystal silicon layers at high temperatures,” *Journal of Applied Physics*, vol. 98, no. 12, p. 123523, Dec. 2005, doi: 10.1063/1.2149497.

[16] H. Inokawa, H. Satoh, and K. Akiba, “Thermal conductance and heat capacity measurement utilizing suspended-wire resistor,” in *2017 15th International Conference on Quality in Research (QiR) :*

*International Symposium on Electrical and Computer Engineering*, Jul. 2017, pp. 124–127. doi: 10.1109/QIR.2017.8168466.

[17] A. Rycerz, "Wiedemann–Franz Law for Massless Dirac Fermions with Implications for Graphene," *Materials*, vol. 14, no. 11, p. 2704, May 2021, doi: 10.3390/ma14112704.

[18] A. Salazar, "On thermal diffusivity," *European Journal of Physics*, vol. 24, no. 4, pp. 351–358, Jul. 2003, doi: 10.1088/0143-0807/24/4/353.

[19] R. Kato and I. Hatta, "Thermal Conductivity and Interfacial Thermal Resistance: Measurements of Thermally Oxidized SiO2 Films on a Silicon Wafer Using a Thermo-Reflectance Technique," *International Journal of Thermophysics*, vol. 29, no. 6, pp. 2062–2071, Dec. 2008, doi: 10.1007/s10765-008-0536-4.

[20] S. Komatsu and M. Ikeda, "Thermal conductivity and electrical resistivity of titanium and its alloys," *Titanium*, vol. 46, no. 4, pp. 1–4, 1998.

[21] A. P. Aji, H. Satoh, C. Apriono, E. T. Rahardjo, and H. Inokawa, "Responsivity Calibration of Terahertz Pyroelectric Detector Based on Blackbody Radiator," in *2021 17th International Conference on Quality in Research (QIR): International Symposium on Electrical and Computer Engineering*, Oct. 2021, pp. 94–97. doi: 10.1109/QIR54354.2021.9716160.

[22] C. Balanis, "Antenna Theory: Analysis and Design," in *Antenna Theory: Analysis and Design*, 4th ed., Hoboken, New Jersey: Wiley, 2016, pp. 75–78.

[23] N. Hiromoto *et al.*, "Room-Temperature Terahertz Antenna-Coupled Microbolometers with Titanium Thermistor and Heater," in *2019 16th International Conference on Quality in Research (QIR): International Symposium on Electrical and Computer Engineering*, Jul. 2019, pp. 1–5. doi: 10.1109/QIR.2019.8898200.

[24] J. Wang, W. Li, J. Gou, Z. Wu, and Y. Jiang, "Fabrication and parameters calculation of room temperature terahertz detector with micro-bridge structure," *Journal of Infrared, Millimeter, and*

*Terahertz Waves*, vol. 36, no. 1, pp. 49–59, Jan. 2015, doi: 10.1007/s10762-014-0120-x.

[25] P. Xiao *et al.*, "Planar double-slot antenna integrated into a Nb5N6 microbolometer THz detector," *Optics Letters*, vol. 45, no. 10, p. 2894, May 2020, doi: 10.1364/ol.388771.

[26] L. Vicarelli, A. Tredicucci, and A. Pitanti, "Micromechanical Bolometers for Subterahertz Detection at Room Temperature," *ACS Photonics*, vol. 9, no. 2, pp. 360–367, Feb. 2022, doi: 10.1021/acsphotonics.1c01273.

[27] S. Bevilacqua and S. Cherednichenko, "Low noise nanometer scale room-temperature YBa2Cu3O7-x bolometers for THz direct detection," *IEEE Transactions on Terahertz Science and Technology*, vol. 4, no. 6, pp. 653–660, Nov. 2014, doi: 10.1109/TTHZ.2014.2344435.

[28] R. Degl'Innocenti *et al.*, "Bolometric detection of terahertz quantum cascade laser radiation with graphene-plasmonic antenna arrays," *Journal of Physics D: Applied Physics*, vol. 50, no. 17, p. 174001, May 2017, doi: 10.1088/1361-6463/aa64bf.

[29] X. Wang, "Monolithic resonant CMOS fully integrated triple-band THz thermal detector," *Optics Express*, vol. 28, no. 15, p. 22630, Jul. 2020, doi: 10.1364/oe.398696.

# *Chapter 4*

# SUMMARY AND FUTURE PROSPECTS

## 4.1 Summary

Numerous applications such as security inspection, wireless communication, food and water quality control, and biomedical diagnosis are suggested for the use of THz spectrum. To widen the scope of THz technology, development of high-sensitivity, low-cost and room-temperature-operating bolometers is anticipated. For the realization of such a bolometer in THz region, the difficulty in thermally isolating the large absorber can be alleviated by the antenna-coupled bolometer structure. Performance enhancement could be expected by the implementation of high-resistance thermistor and heater, suggested the use of high-impedance antenna. The main objective of this thesis is to investigate the performance of bolometer with high-resistance heater and high-impedance folded dipole antenna (FDA) for THz bolometer applications.

In ***Chapter 1***, the exciting features of THz region and its application in various fields were discussed briefly. The interesting properties of THz spectrum such as, high penetration capability, non-ionizing, high-intensity, high-resolution, and "THz fingerprints" were discussed along with

prospective THz applications. Common classification of THz detectors such as photon and thermal detectors, and electronic receivers were discussed. The motivation of present study and synopsis of this thesis chapters are provided.

In ***Chapter 2***, the FDAs were designed and simulated with various geometries at 1 THz frequency. The FDA could yield high input impedance characteristic up to 1.5 kΩ with the proper selection of length, width, spacing between arms, and number of arms. Simulation in receiving mode reveals that the responsivity improvement in THz bolometer could be attained from the product of antenna area efficiency and resonant resistance with the optimum performance is obtained from the 3-arms FDA with 1-μm wide and 4-μm space between arms. A comparison with half-wave dipole antenna was made to justify the improvement by FDA, based on the assumption that heater resistance is dominating the thermal resistance of entire detector and responsivity is proportional to the heater resistance increase.

In ***Chapter 3***, fabrication and measurements of antenna-coupled bolometer were discussed. Bolometer with various heater width were fabricated with a common 0.1-μm-wide meander thermistor. Folded dipole antenna was investigated by coupling it to high-resistance heater.

Comparison was made with the low resistance heater coupled to a halfwave dipole antenna. From the electrical measurement results, responsivity and NEP performance can be improved simultaneously up to 2.5 times by increasing heater resistance. Thermal resistance analysis was taken by an analytic circuit model that fit to the measurement results, suggesting the effectiveness of the model to predict the bolometer performance. Optical measurement results reveal the improvement of responsivity by using folded dipole antenna with high heater resistance, compared to the halfwave dipole antenna.

## 4.2 Future Prospect

The research objective presented in this thesis was to analyze the improvement of heater resistance to the bolometer responsivity, and application of folded dipole antenna coupled with high-resistance heater. However, we find that the performance improvement attained in both electrical and optical measurements are not so high as we initially expected based on the assumption that the heater dominates the thermal conduction in the detector. Since the objective of this thesis has been partially achieved, there remains a room for improvement. Thermal resistance could be further increased by minimizing the thermal conduction by other parts than the heater, such as thermistor and $SiO_2$ inter/base layer. By using a

single metallic film as heater and thermistor, and eliminating the $SiO_2$ inter/base layer, thermal resistance can be increased as predicted by the scaling study in Chapter 1. However, careful comparison with the separate heater/ thermistor structure has to be made based on the available high impedance by the existing antennas.

## *List of Journal Publications and Conference Proceedings*

### Journal Publication

1) A. P. Aji, H. Satoh, C. Apriono, E. T. Rahardjo and H. Inokawa, "Responsivity and NEP Improvement of THz Microbolometer by High-impedance Antenna," Sensors 2022, 22, 5107. DOI:10.3390/s22145107. Scopus Q2 IF = 3.847 (2022)

### List of Conference Proceedings

1) A. P. Aji, H. Satoh, C. Apriono, E. T. Rahardjo and H. Inokawa, "Investigation of High-Impedance Antenna for Terahertz Microbolometer," in *Proceeding of the 1st International Conference of Electronics, Photonics and Smart Technologics (ICePhaST) 2020*. (*presented*) Online, November 16, 2020.

2) A. P. Aji, H. Satoh, C. Apriono, E. T. Rahardjo, N. Hiromoto and H. Inokawa, "Performance Improvement of THz Microbolometer by Folded - Dipole Antenna," in *68th spring meeting, Japan Society of Applied Physics*, 18p-Z09-2. (presented) Online, March 18, 2021.

3) A. P. Aji, H. Satoh, C. Apriono, E. T. Rahardjo and H. Inokawa, "Length and space dependence of heater power dissipation in folded-dipole antenna for terahertz microbolometer," in *International*

*Symposium towards the Future of Advanced Researches (ISFAR) 2021*. (*presented*) Hamamatsu, March 5, 2021.

4) A. P. Aji, H. Satoh, C. Apriono, E. T. Rahardjo and H. Inokawa, "Responsivity Calibration of Terahertz Pyroelectric Detector Based on Blackbody Radiator," in *Proceedings of the 2021 International Conference on Quality in Research (QIR): International Symposium on Electrical and Computer Engineering*. (*presented*), Online, October 13, 2021.